

Accurate Biot-Savart Routines with Correct Asymptotic Behavior

Jonathan Schilling^{a,*}, Jakob Svensson^a, Udo Höfel^a, Joachim Geiger^a,
Henning Thomsen^a

^a*Max-Planck-Institute for Plasma Physics, Wendelsteinstrasse 1, 17491 Greifswald,
Germany*

Abstract

A set of routines to compute the magnetic vector potential and magnetic field of two types of current carriers is presented. The (infinitely thin) current carrier types are a straight wire segment and a circular wire loop. The routines are highly accurate and exhibit the correct asymptotic behavior far away from and close to the current carrier. A suitable global set of test points is introduced and the methods presented in this work are tested against results obtained using arbitrary-precision arithmetic on all test points. The results are accurate to approximately 16 decimal digits of precision when computed using 64 bit floating point arithmetic. There are a few exceptions where accuracy drops to 13 digits. These primitive current carrier types can be used to assemble more complex arrangements, such as a current along a polygon (by means of defining straight wire segments from point to point along the polygon) and a multi-winding coil with circular cross-section. Reference data is provided along with the code for benchmarks with other implementations.

Keywords: magnetostatics; Biot-Savart; straight wire segment; circular wire loop; magnetic vector potential; magnetic field

PROGRAM SUMMARY

Program Title: Accurate Biot-Savart routines with Correct Asymptotic Behavior

CPC Library link to program files: (to be added by Technical Editor)

Developer's repository link: <https://github.com/jonathanschilling/abscab>

*Corresponding author.

E-mail address: jonathan.schilling@ipp.mpg.de

Code Ocean capsule: (to be added by Technical Editor)

Licensing provisions: Apache-2.0

Programming language: C, Python, Java, Fortran

Supplementary material: Reference output data for all methods described in this article.

Nature of problem:

A common task in computational physics is to compute the magnetic field and magnetic vector potential originating from current-carrying wire arrangements in the form of coils and cables. These current carriers can be approximated for computational simplicity as infinitely thin filaments following the center lines of the real current carrier. A current carrier path specified by a list of points along the path can be modeled as a set of straight wire segments from point to point along the polygon describing the current carrier geometry. Closed circular wire loops appear as well in practise and can be chosen to model, e.g., individual windings in a circular coil. Computational methods are thus needed to compute the magnetic field and the magnetic vector potential of a single straight wire segment or a single circular wire loop in order to model more complex current carrier arrangements by superposition of the current carrier primitives.

Solution method:

Analytical expressions are derived in this work to accurately compute the magnetic field and the magnetic vector potential of a straight wire segment and a circular wire loop. The expressions consist of several special cases, which are switched between depending on the location of the evaluation location in the coordinate system of the current carrier primitive. This approach allows to select the most accurate formulation for a given evaluation location and to make explicit use of simplifications in certain special cases for speed and accuracy. Particular attention was paid to ensure that the expressions presented in this work obey the correct asymptotic behavior for evaluation locations far away from and close to the current carriers.

Additional comments including restrictions and unusual features:

For most test cases, the full relative accuracy of the floating point arithmetic chosen for implementation is retained throughout the computations (16 digits of precision in the IEEE-754 `binary64` implementation). There are a few exceptions where accuracy drops by up to 3 digits of precision (in the `binary64` case). The provided implementations have not been optimized for speed.

1. Introduction

A common task in computational physics is to compute the magnetic field and magnetic vector potential originating from current-carrying wire arrangements. These current carriers are often approximated for computational simplicity as infinitely thin filaments following the center lines of the real current carrier. A current carrier path specified by (x,y,z) coordinates can be modeled as a set of straight wire segments from point to point along the polygon describing the current carrier geometry. Closed circular wire loops are also commonly used as a proxy for a physical coil with helical windings. Computational methods are needed to compute the magnetic field and the magnetic vector potential of a single straight wire segment or a single circular wire loop in order to model more complex current carrier arrangements by superposition of the current carrier primitives. Analytical expressions are derived in this work to accurately compute the magnetic field and the magnetic vector potential of a straight wire segment and a circular wire loop. The expressions consist of several special cases, which are switched between depending on the location of the evaluation location in the coordinate system of the current carrier primitive. This approach allows to select the most accurate formulation for a given evaluation location and to make explicit use of simplifications in certain special cases for speed and accuracy. The provided implementations have not been optimized for speed.

The magnetic vector field is denoted by \mathbf{H} and the magnetic flux density \mathbf{B} is then given by $\mathbf{B} = \mu_0\mu_r\mathbf{H}$, where μ_0 is the vacuum magnetic permeability and μ_r is the relative permeability, taking material properties into account. Generally, in the field of plasma physics and in particular in this work, these two terms are frequently used synonymously due to the vanishing magnetic susceptibility $|\chi| \ll 1$ of the plasma, leading to $\mu_r = 1 + \chi \approx 1$. This is equivalent to considering only vacuum magnetic fields. In this case, the magnetic field and magnetic flux density only differ by a factor of μ_0 .

The paper is structured as follows. In section 2, the main numerical method of this work is presented together with arbitrary-precision reference calculations to benchmark the numerical method. The results of the comparison between the finite-precision method and the arbitrary-precision reference data are presented in Sec. 3 and then further discussed in Sec. 4. An outlook is given in Sec. 5. The full derivations of the equations presented in this work are given in Appendix A.

2. Methods

In this section, accurate methods used to compute the magnetic vector potential \mathbf{A} and the magnetic field \mathbf{B} of a straight wire segment and a circular wire loop are presented. Furthermore, methods to evaluate the magnetostatic quantities in global coordinates are provided. Particular attention was paid to ensure that the expressions presented in this work obey the correct asymptotic behavior for evaluation locations far away from and close to the current carriers. For most test cases, the full relative accuracy of the floating point arithmetic chosen for implementation is retained throughout the computations (16 digits of precision in the IEEE-754 `binary64` [1] implementation). There are a few exceptions where accuracy drops by up to 3 digits of precision (in the `binary64` case). The section concludes with a description of the verification procedure employed to benchmark these methods.

2.1. Straight Wire Segment

The basic geometry of a single wire segment is shown in Fig. 1. A cylindrical coordinate system (ρ, φ, z) is aligned with the wire segment (red line), such that the wire is aligned with the z -axis and starts at the origin. A current I flows along the wire segment of length L in positive z direction (red arrow). The evaluation point is specified by $\mathbf{x} = (\rho, \varphi = 0, z)$. R_i (R_f) denotes the distance from the start (end) of the wire segment to \mathbf{x} . The angles α and β are used in the formulas below.

2.1.1. Magnetic Vector Potential

The magnetic vector potential of a straight wire segment only has component A_z parallel to the wire:

$$\mathbf{A} = A_z \hat{\mathbf{e}}_z \quad (1)$$

where $\hat{\mathbf{e}}_z$ is the unit vector in direction z . It is given by [2]:

$$A_z(\rho, z) = \frac{\mu_0 I}{4\pi} \ln \left(\frac{1 + \epsilon}{1 - \epsilon} \right) \quad (2)$$

with

$$\epsilon = \frac{L}{R_i + R_f} \quad (3)$$

$$R_i = \sqrt{\rho^2 + z^2} \quad (4)$$

$$R_f = \sqrt{\rho^2 + (1 - z)^2}. \quad (5)$$

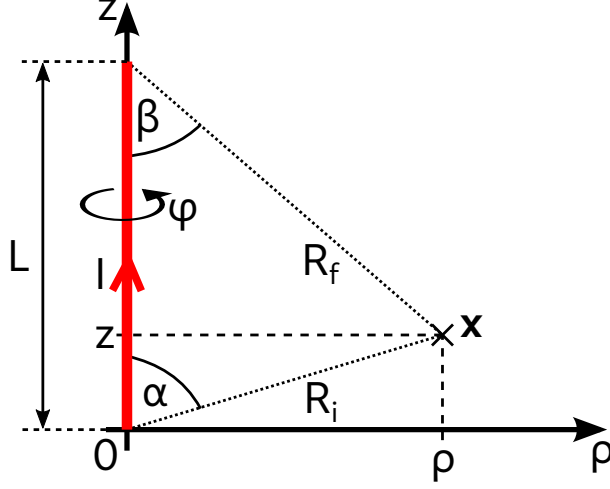


Figure 1: Geometry of a single wire segment (red line) and the associated cylindrical coordinate system. The magnetostatic quantities are to be evaluated at a location \mathbf{x} . After Fig. 1 in Ref. [2].

In this work normalized coordinates $\rho' = \rho/L$ and $z' = z/L$ are used. This leads to the following expressions for $r_i = R_i/L$ and $r_f = R_f/L$:

$$r_i = \sqrt{\rho'^2 + z'^2} \quad (6)$$

$$r_f = \sqrt{\rho'^2 + (1 - z')^2} \quad (7)$$

$$\Rightarrow \epsilon = \frac{1}{r_i + r_f} . \quad (8)$$

For locations on the conductor, $\epsilon = 1$ holds. The magnetostatic quantities can only be evaluated at points not located on the conductor, where $\epsilon < 1$ holds. The value of ϵ only depends on the sum $R_i + R_f$, which implies that contours of constant ϵ are ellipses with foci at the ends of the wire segment. This is similar to the Gardener's construction method for ellipses [3]. The elliptical contours of constant ϵ are illustrated in Fig. 2. The contours approach a circular shape far away from the wire segment. A common prefactor depending on the current I and μ_0 is split off:

$$A_z(\rho', z') = \frac{\mu_0 I}{2\pi} \tilde{A}_z(\rho', z') \quad (9)$$

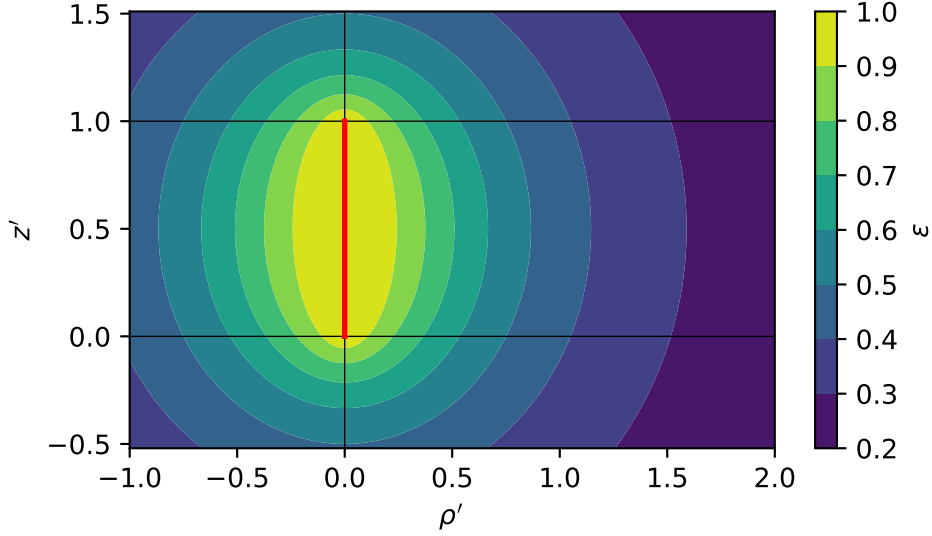


Figure 2: Contours of constant ϵ as computed from Eqn. (8). The straight wire segment is located along the red line.

with

$$\tilde{A}_z(\rho', z') = \frac{1}{2} \ln \left(\frac{1 + \epsilon}{1 - \epsilon} \right) = \text{atanh}(\epsilon). \quad (10)$$

The rest of this section is dedicated to the accurate computation of $\tilde{A}_z(\rho', z')$. One of several formulations is chosen depending on the evaluation location (ρ', z') :

$$\tilde{A}_z(\rho', z') = \begin{cases} \tilde{A}_{z,\text{ax}}(z') & : \rho' = 0, \text{ any } z' \notin [0, 1] \\ \tilde{A}_{z,\text{rad}}(\rho') & : 0 < \rho' < 1, z' \in \{0, 1\} \\ \tilde{A}_{z,\text{f}}(\rho', z') & : \rho' \geq 1 \text{ or } z' \leq -1 \text{ or } z' > 2 \\ \tilde{A}_{z,\text{n}}(\rho', z') & : \text{elsewhere.} \end{cases} \quad (11)$$

The domain decomposition used to compute \tilde{A}_z accurately is depicted in Fig. 3(a). The case $\rho' = 0$ is considered first. Recall that the wire segment extends along $\rho' = 0$ from $z' = 0$ to $z' = 1$. The magnetostatic quantities are well-defined for $\rho' = 0$ as long as $z' < 0$ or $z' > 1$. For the case $\rho' = 0$, the following formulation is used for valid evaluation locations:

$$\tilde{A}_{z,\text{ax}}(z') = \begin{cases} \tilde{A}_{z,\text{ax},\text{f}}(z') & : z' < -1 \text{ or } z' \geq 2 \\ \tilde{A}_{z,\text{ax},\text{n}}(z') & : -1 \leq z' < 0 \text{ or } 1 < z' < 2 \end{cases} \quad (12)$$

with

$$\tilde{A}_{z,\text{ax},f}(z') = \text{atanh} \left(\frac{1}{|z'| + |1 - z'|} \right) \quad (13)$$

and

$$\tilde{A}_{z,\text{ax},n}(z') = \frac{1}{2} \frac{z'}{|z'|} \ln \left(\left| \frac{z'}{1 - z'} \right| \right). \quad (14)$$

The following formulation is used for the cases $z' = 0$ or $z' = 1$:

$$\tilde{A}_{z,\text{rad}}(\rho') = \begin{cases} \tilde{A}_{z,\text{rad},f}(\rho') & : \rho' > 1 \\ \tilde{A}_{z,\text{rad},n}(\rho') & : 0 < \rho' \leq 1 \end{cases} \quad (15)$$

with

$$\tilde{A}_{z,\text{rad},f}(\rho') = \text{atanh} \left(\frac{1}{\rho' + \sqrt{\rho'^2 + 1}} \right) \quad (16)$$

and

$$\tilde{A}_{z,\text{rad},n}(\rho') = \frac{1}{2} \ln \left(\frac{\rho'c + 1 + c}{\rho'c + 2s^2} \right), \quad (17)$$

where

$$c = \frac{1}{\sqrt{\rho'^2 + 1}} \quad (18)$$

$$s = \sin(\arctan(\rho')/2). \quad (19)$$

The case of $\tilde{A}_{z,f}(\rho', z')$ is implemented as:

$$\tilde{A}_{z,f}(\rho', z') = \text{atanh}(\epsilon) \quad (20)$$

with r_i , r_f and ϵ from Eqn. (6), Eqn. (7) and Eqn. (8), respectively. The final case is implemented as follows:

$$\tilde{A}_{z,n}(\rho', z') = \frac{1}{2} [\ln(n + 2) - \ln(n)] \quad (21)$$

with

$$n = (r_i - z') + (r_f - (1 - z')) \quad (22)$$

$$r_i - z' = 2r_i \sin^2(\alpha/2) \quad (23)$$

$$r_f - (1 - z') = 2r_f \sin^2(\beta/2) \quad (24)$$

$$\alpha = \text{atan2}(\rho', z') \quad (25)$$

$$\beta = \text{atan2}(\rho', 1 - z') \quad (26)$$

and r_i , r_f from Eqn. (6), Eqn. (7), respectively.

2.1.2. Magnetic Field

The magnetic field of a straight wire segment is given by the law of Biot and Savart as follows [2]:

$$\mathbf{B} = \frac{\mu_0 I}{4\pi} \hat{\mathbf{e}}_z \times \mathbf{R}_i \frac{2L(R_i + R_f)}{R_i R_f} \frac{1}{(R_i + R_f)^2 - L^2}. \quad (27)$$

The vector \mathbf{R}_i has components in directions parallel (z) and perpendicular (ρ) to the wire segment:

$$\mathbf{R}_i = z \hat{\mathbf{e}}_z + \rho \hat{\mathbf{e}}_\rho \quad (28)$$

where ρ and z are cylindrical coordinates in the coordinate system aligned with the wire segment. The vector-valued term in Eqn. (27) is reformulated as follows by inserting Eqn. (28):

$$\begin{aligned} \hat{\mathbf{e}}_z \times \mathbf{R}_i &= \hat{\mathbf{e}}_z \times (z \hat{\mathbf{e}}_z + \rho \hat{\mathbf{e}}_\rho) \\ &= z \underbrace{\hat{\mathbf{e}}_z \times \hat{\mathbf{e}}_z}_{=0} + \rho \underbrace{\hat{\mathbf{e}}_z \times \hat{\mathbf{e}}_\rho}_{=\hat{\mathbf{e}}_\varphi} = \rho \hat{\mathbf{e}}_\varphi. \end{aligned} \quad (29)$$

It follows that the magnetic field of a straight wire segment only has a component B_φ in tangential (φ) direction:

$$\mathbf{B} = B_\varphi \hat{\mathbf{e}}_\varphi \quad (30)$$

with

$$B_\varphi(\rho, z) = \frac{\mu_0 I}{4\pi} \frac{2\rho L(R_i + R_f)}{R_i R_f} \frac{1}{(R_i + R_f)^2 - L^2}. \quad (31)$$

This is now reformulated to use normalized coordinates (as done above for the computation of the magnetic vector potential):

$$B_\varphi(\rho', z') = \frac{\mu_0 I}{4\pi L} \left(\frac{1}{r_f} + \frac{1}{r_i} \right) \frac{2\rho'}{(r_i + r_f)^2 - 1}. \quad (32)$$

Again a normalization factor is split off:

$$B_\varphi(\rho', z') = \frac{\mu_0 I}{4\pi L} \tilde{B}_\varphi(\rho', z') \quad (33)$$

with

$$\tilde{B}_\varphi(\rho', z') = \left(\frac{1}{r_f} + \frac{1}{r_i} \right) \frac{2\rho'}{(r_i + r_f)^2 - 1}. \quad (34)$$

Consider the denominator in more detail:

$$\begin{aligned}
(r_i + r_f)^2 - 1 &= r_i^2 + 2r_i r_f + r_f^2 - 1 \\
&= \rho'^2 + z'^2 + 2r_i r_f + \rho'^2 + (1 - z')^2 - 1 \\
&= \rho'^2 + z'^2 + 2r_i r_f + \rho'^2 - 1 - 2z' + z'^2 - 1 \\
&= 2\rho'^2 + 2z'^2 + 2r_i r_f - 2z' \\
&= 2 \left[\rho'^2 + r_i r_f - z'(1 - z') \right] .
\end{aligned} \tag{35}$$

This leads to:

$$\tilde{B}_\varphi(\rho', z') = \left(\frac{1}{r_f} + \frac{1}{r_i} \right) \frac{\mathfrak{Z}\rho'}{\mathfrak{Z} \left[\rho'^2 + r_i r_f - z'(1 - z') \right]} . \tag{36}$$

One of several formulations is chosen depending on the evaluation location (ρ', z') :

$$\tilde{B}_\varphi(\rho', z') = \begin{cases} 0 & : \rho' = 0, \text{ any } z' \\ \tilde{B}_{\varphi, \text{rad}}(\rho') & : \rho' > 0, z' \in \{0, 1\} \\ \tilde{B}_{\varphi, \text{f}}(\rho', z') & : \rho' \geq 1 \text{ or } z' \leq 0 \text{ or } z' \geq 1 \\ & \text{or } \rho'/(1 - z') \geq 1 \\ & \text{or } \rho'/z' \geq 1 \\ \tilde{B}_{\varphi, \text{n}}(\rho', z') & : \text{else.} \end{cases} \tag{37}$$

The domain decomposition used to compute \tilde{B}_φ accurately is depicted in Fig. 3(b). The special case $z' \in \{0, 1\}$ is implemented as follows:

$$\tilde{B}_{\varphi, \text{rad}}(\rho') = \frac{1}{\rho' \sqrt{\rho'^2 + 1}} . \tag{38}$$

The formula in Eqn. (36) is used for evaluation locations far away from the wire as well as a part of the near-field close to the wire segment:

$$\tilde{B}_{\varphi, \text{f}}(\rho', z') = \left(\frac{1}{r_f} + \frac{1}{r_i} \right) \frac{\rho'}{\rho'^2 + r_i r_f - z'(1 - z')} . \tag{39}$$

The final case is implemented as follows:

$$\tilde{B}_{\varphi, \text{n}}(\rho', z') = \left(\frac{1}{r_f} + \frac{1}{r_i} \right) \frac{\rho'}{\rho'^2 + 2r_i \left[r_f \sin^2(\beta/2) + (1 - z') \sin^2(\alpha/2) \right]} \tag{40}$$

with α and β from Eqn. (25) and Eqn. (26), respectively.

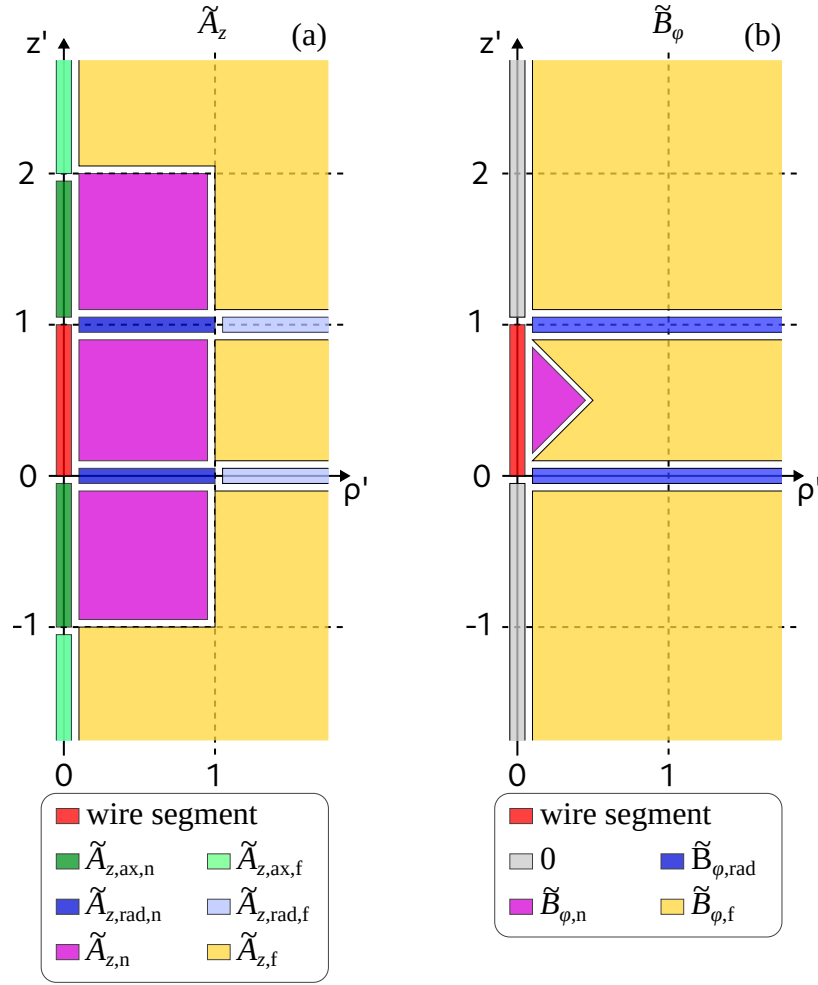


Figure 3: Domain decomposition used to partition the evaluation region for computing \tilde{A}_z (a) and \tilde{B}_ϕ (b) accurately. The colored regions indicate at which evaluation locations (ρ', z') which formulation (see legend) is used.

2.2. Circular Wire Loop

The basic geometry of a circular wire loop under consideration here is shown in Fig. 4. The loop is centered at the origin with its normal vector aligned with the z -axis. The radius of the loop is denoted a and a current I (with corresponding current density \mathbf{j}) flows in the direction indicated in Fig. 4. The magnetic field and vector potential are to be evaluated at the point \mathbf{x} in the (x, z) -plane. The coordinates of the evaluation point can be expressed in spherical coordinates as (r, θ) or in cylindrical coordinates as (ρ, z) . The axisymmetry of this setup always allows to rotate the coordinate system such that $\varphi = 0$ can be assumed. Similar to the case of the

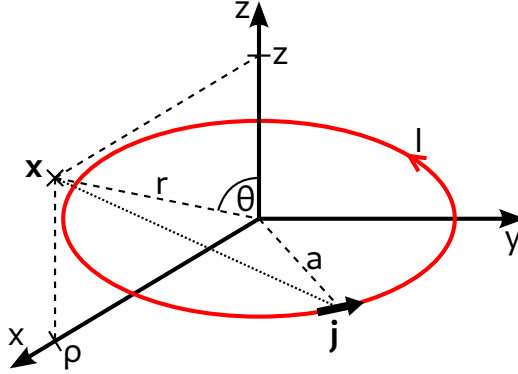


Figure 4: Geometry of a circular wire loop centered at the origin with normal vector aligned with the z -axis.

straight wire segment, the magnetic vector potential and the magnetic field of the circular wire loop are assembled from various formulations for special cases of the far-field and the near-field in the implementation described later.

2.2.1. Magnetic Vector Potential

The magnetic vector potential of a circular wire loop only has a tangential component A_φ . In Eqn. (5.37) of Ref. [4], A_φ is expressed as follows for a loop of radius a and current I along it:

$$A_\varphi(r, \theta) = \frac{\mu_0}{4\pi} \frac{4Ia}{\sqrt{a^2 + r^2 + 2ar \sin(\theta)}} \left[\frac{(2 - k^2)\mathcal{K}(k) - 2\mathcal{E}(k)}{k^2} \right] \quad (41)$$

with

$$k^2 = \frac{4ar \sin(\theta)}{a^2 + r^2 + 2ar \sin(\theta)}. \quad (42)$$

Here, $\mathcal{K}(k)$ and $\mathcal{E}(k)$ are the complete elliptic integrals of the first and second kind, respectively. Spherical coordinates (r, θ) are used to specify the evaluation location. The corresponding cylindrical coordinates (ρ, z) are given by $\rho = r \sin(\theta)$ and $z = \sqrt{r^2 - \rho^2}$. Normalized coordinates (ρ', z') are introduced with

$$\rho' = \rho/a \quad (43)$$

$$z' = z/a. \quad (44)$$

An expression for the linear combination of $\mathcal{K}(k)$ and $\mathcal{E}(k)$ is used to reformulate Eqn. (41):

$$\lambda \mathcal{K}(k) + \mu \mathcal{E}(k) = \text{cel}(k_c, 1, \lambda + \mu, \lambda + \mu k_c^2) \quad (45)$$

where

$$k_c^2 = 1 - k^2 \quad (46)$$

and cel is the so-called general complete elliptic integral introduced by Bulirsch [5]:

$$\text{cel}(k_c, p, a, b) = \int_0^{\pi/2} \frac{a \cos^2(\varphi) + b \sin^2(\varphi)}{\cos^2(\varphi) + p \sin^2(\varphi)} \frac{d\varphi}{\sqrt{\cos^2(\varphi) + k_c^2 \sin^2(\varphi)}}. \quad (47)$$

The argument of the elliptic integrals is considered first:

$$\begin{aligned} k^2 &= \frac{4ar \sin(\theta)}{a^2 + r^2 + 2ar \sin(\theta)} = \frac{4a\rho}{a^2 + r^2 + 2a\rho} = \frac{4a\rho}{a^2 \left(1 + \frac{r^2}{a^2} + 2\frac{\rho}{a}\right)} \\ &= \frac{4\rho'}{1 + \frac{r^2}{a^2} + 2\rho'} = 4\rho' \left(1 + \frac{\rho'^2 + z'^2}{a^2} + 2\rho'\right)^{-1} \\ &= 4\rho' (1 + \rho'^2 + z'^2 + 2\rho')^{-1} = \frac{4\rho'}{z'^2 + (1 + \rho')^2}. \end{aligned} \quad (48)$$

This implies:

$$k_c^2 = \frac{z'^2 + (1 - \rho')^2}{z'^2 + (1 + \rho')^2}. \quad (49)$$

The coefficients of the elliptic integrals in Eqn. (41) are identified as follows:

$$\lambda = \frac{2 - k^2}{k^2} = \frac{2}{k^2} - 1 \quad (50)$$

$$\mu = -\frac{2}{k^2} \quad (51)$$

and their combinations are as follows for use in Eqn. (45):

$$\lambda + \mu = \frac{2}{k^2} - 1 - \frac{2}{k^2} = -1 \quad (52)$$

$$\begin{aligned} \lambda + \mu k_c^2 &= \frac{2}{k^2} - 1 - \frac{2}{k^2}(1 - k^2) \\ &= \frac{2}{k^2} - 1 - \frac{2}{k^2} + 2 = 1. \end{aligned} \quad (53)$$

Putting Eqn.s (45) to (53) together, we arrive at the following expression for A_φ :

$$A_\varphi(\rho', z') = \frac{\mu_0 I}{\pi} \frac{1}{\sqrt{z'^2 + (1 + \rho')^2}} \text{cel}(k_c, 1, -1, 1). \quad (54)$$

It is favorable for numerical evaluation of A_φ to use the form given in Eqn. (54) where the linear combination of the complete elliptic integrals is embedded in the parameters of cel and less precautions need to be taken to deal with cancellations in Eqn. (41). A physics-oriented prefactor is split off to be able to focus on geometry in the following:

$$A_\varphi(\rho', z') = \frac{\mu_0 I}{\pi} \tilde{A}_\varphi(\rho', z') \quad (55)$$

with

$$\tilde{A}_\varphi(\rho', z') = \frac{1}{\sqrt{z'^2 + (1 + \rho')^2}} \text{cel}(k_c, 1, -1, 1). \quad (56)$$

One of several formulations for \tilde{A}_φ is chosen depending on the evaluation location (ρ', z') :

$$\tilde{A}_\varphi(\rho', z') = \begin{cases} 0 & : \rho' = 0, \text{ any } z' \\ \tilde{A}_{\varphi,\text{f}}(\rho', z') & : 0 < \rho' < 1/2 \text{ or } \rho' > 2 \text{ or } |z'| \geq 1 \\ \tilde{A}_{\varphi,\text{n}}(\rho', z') & : 1/2 \leq \rho' \leq 2 \text{ but } \rho' \neq 1, |z'| < 1 \\ \tilde{A}_{\varphi,\text{v}}(z') & : \text{else } (\rho' = 1, |z'| < 1). \end{cases} \quad (57)$$

The domain decomposition used to compute \tilde{A}_φ accurately is depicted in Fig. 5. The following formula is implemented for evaluation locations away from the wire loop:

$$\tilde{A}_{\varphi,\text{f}}(\rho', z') = \frac{k^2}{\sqrt{z'^2 + (1 + \rho')^2}} \mathcal{C}(k_c) \quad (58)$$

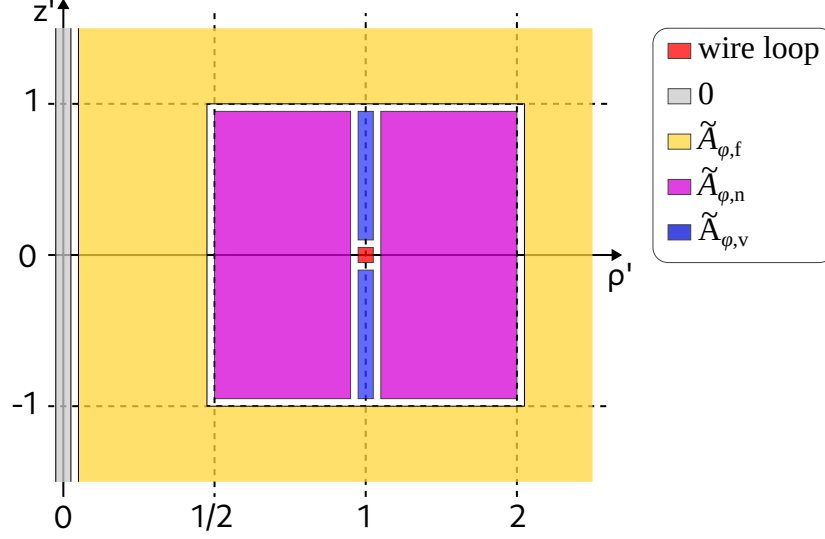


Figure 5: Domain decomposition used to partition the evaluation region for computing \tilde{A}_φ accurately. The colored regions indicate at which evaluation locations (ρ', z') which formulation (see legend) is used.

with k^2 from Eqn. (48) and

$$\mathcal{C}(k_c) = \text{cel} \left(\frac{2\sqrt{k_c}}{1+k_c}, 1, 0, \frac{2}{(1+k_c)^3} \right). \quad (59)$$

Close to the wire loop, the following formulation is used:

$$\tilde{A}_{\varphi,n}(\rho', z') = \frac{1}{|\rho' - 1| \sqrt{\left(\frac{z'}{\rho'-1}\right)^2 + \left(1 + \frac{2}{\rho'-1}\right)^2}} \text{cel}(\sqrt{k_c^2}, 1, -1, 1) \quad (60)$$

with k_c^2 computed as follows:

$$k_c^2 = \frac{\left(\frac{z'}{\rho'-1}\right)^2 + 1}{\left(\frac{z'}{\rho'-1}\right)^2 + \left(1 + \frac{2}{\rho'-1}\right)^2}. \quad (61)$$

At $\rho' = 1$, some further simplification can be carried out. This leads to the following formulation for $\rho' = 1$ and $|z'| < 1$:

$$\tilde{A}_{\varphi,v}(z') = \frac{1}{|z'|} \text{cel} \left(\frac{1}{k_c}, 1, 1, -1 \right) \quad (62)$$

with k_c computed as follows:

$$k_c = \frac{|z'|}{\sqrt{4 + z'^2}}. \quad (63)$$

2.2.2. Magnetic Field

The magnetic field produced by a circular wire loop is made up of two components:

$$\mathbf{B} = B_\rho \hat{\mathbf{e}}_\rho + B_z \hat{\mathbf{e}}_z \quad (64)$$

where B_ρ denotes the radial component and B_z denotes the vertical component. The radial component B_ρ is given by [6]:

$$B_\rho(\rho', z') = \frac{\mu_0 I}{\pi a} \frac{z'}{[z'^2 + (1 + \rho')^2]^{3/2}} \text{cel}(k_c, k_c^2, -1, 1) \quad (65)$$

Also here, a normalization factor is split off:

$$B_\rho(\rho', z') = \frac{\mu_0 I}{\pi a} \tilde{B}_\rho(\rho', z') \quad (66)$$

with

$$\tilde{B}_\rho(\rho', z') = \frac{z'}{[z'^2 + (1 + \rho')^2]^{3/2}} \text{cel}(k_c, k_c^2, -1, 1). \quad (67)$$

One of several formulations is chosen depending on the evaluation location (ρ', z') :

$$\tilde{B}_\rho(\rho', z') = \begin{cases} 0 & : \rho' = 0, \text{ any } z' \\ & \text{or } \rho' > 0, z' = 0 \\ \tilde{B}_{\rho, \text{f}}(\rho', z') & : \rho' < 1/2 \text{ or } \rho' > 2 \text{ or } |z'| \geq 1 \\ \tilde{B}_{\rho, \text{n}}(\rho', z') & : 1/2 \leq \rho' \leq 2 \text{ but } \rho' \neq 1, |z'| < 1 \\ \tilde{B}_{\rho, \text{v}}(z') & : \text{else } (\rho' = 1, |z'| < 1). \end{cases} \quad (68)$$

The domain decomposition used to compute \tilde{B}_ρ accurately is depicted in Fig. 6. The following formulation is implemented for evaluation locations away from the wire loop:

$$\tilde{B}_{\rho, \text{f}}(\rho', z') = \frac{4\rho' z' [\mathcal{D}(k_c) - \mathcal{C}(k_c)]}{[z'^2 + (1 + \rho')^2]^{3/2} [z'^2 + (1 - \rho')^2]} \quad (69)$$

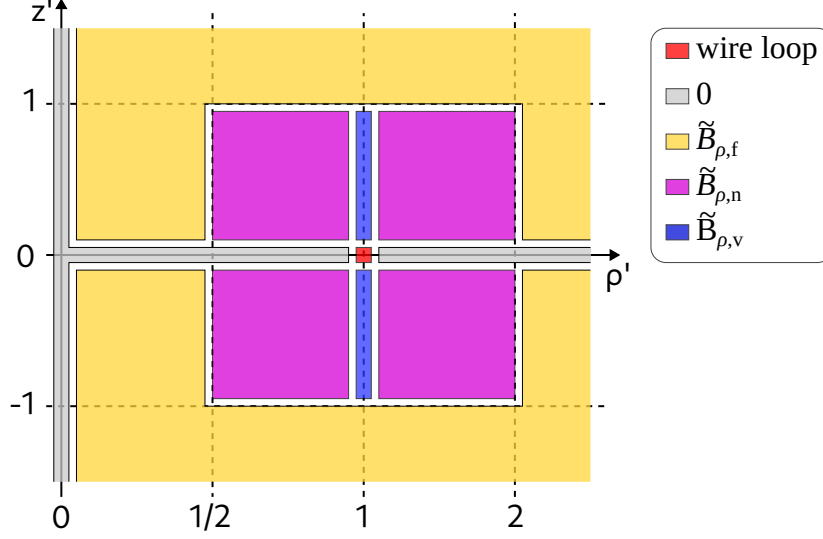


Figure 6: Domain decomposition used to partition the evaluation region for computing \tilde{B}_ρ accurately. The colored regions indicate at which evaluation locations (ρ', z') which formulation (see legend) is used.

with

$$\mathcal{D}(k_c) = \frac{\mathcal{K}(k) - \mathcal{E}(k)}{k^2} = \text{cel}(k_c, 1, 0, 1). \quad (70)$$

For points close to the wire loop, but with $\rho' \neq 1$, the following formulation is used:

$$\tilde{B}_{\rho,n}(\rho', z') = \frac{4\rho' \left| \frac{z'}{\rho'-1} \right| [\mathcal{D}(k_c) - \mathcal{C}(k_c)]}{(\rho' - 1)^4} \left\{ \left[\left(\frac{z'}{\rho'-1} \right)^2 + \left(1 + \frac{2}{\rho'-1} \right)^2 \right]^{3/2} \left[\left(\frac{z'}{\rho'-1} \right)^2 + 1 \right] \right\}^{-1}. \quad (71)$$

Finally, for $\rho' = 1$ and $|z'| < 1$, the following formulation is used:

$$\tilde{B}_{\rho,v}(z') = \frac{k_c}{2} \frac{z'}{|z'|} \left[\left(\frac{2}{z'^2} + 1 \right) \mathcal{E}(k_c) - \mathcal{K}(k_c) \right] \quad (72)$$

with

$$k_c^2 = \frac{1}{1 + 4/z'^2} \quad (73)$$

and

$$\mathcal{K}(k_c) = \text{cel}(k_c, 1, 1, 1) \quad (74)$$

$$\mathcal{E}(k_c) = \text{cel}(k_c, 1, 1, k_c^2). \quad (75)$$

The vertical component B_z of the magnetic field of a circular wire loop is given by [6]:

$$B_z(\rho', z') = \frac{\mu_0 I}{2\pi a} \frac{1}{\rho' \sqrt{z'^2 + (1 + \rho')^2}} \left[\text{cel}(k_c, 1, -1, 1) + \frac{1 + k_c^2 - (1 - k_c^2) \rho'}{2} \text{cel}(k_c, k_c^2, -1, 1) \right] \quad (76)$$

A normalization factor is split off here as well:

$$B_z(\rho', z') = \frac{\mu_0 I}{\pi a} \tilde{B}_z(\rho', z') \quad (77)$$

with

$$\tilde{B}_z(\rho', z') = \frac{1}{2\rho' \sqrt{z'^2 + (1 + \rho')^2}} \left[\text{cel}(k_c, 1, -1, 1) + \frac{1 + k_c^2 - (1 - k_c^2) \rho'}{2} \text{cel}(k_c, k_c^2, -1, 1) \right]. \quad (78)$$

The evaluation of this formula is split up as well into separate special cases. One of several formulations is selected depending on the evaluation location (ρ', z') :

$$\tilde{B}_z(\rho', z') = \begin{cases} \tilde{B}_{z,\text{fl}}(\rho', z') & : \rho' < 1/2, \text{ any } z' \\ & \text{or } \rho' \leq 2, |z'| > 1 \\ \tilde{B}_{z,\text{f2}}(\rho', z') & : \rho' > 2, \text{ any } z' \\ \tilde{B}_{z,\text{n}}(\rho', z') & : 1/2 \leq \rho' \leq 2 \text{ but } \rho' \neq 1, |z'| \leq 1 \\ \tilde{B}_{z,\text{v}}(z') & : \text{else } (\rho' = 1, |z'| \leq 1). \end{cases} \quad (79)$$

The domain decomposition used to compute \tilde{B}_z accurately is depicted in Fig. 7. For points not too close to the wire loop and with $\rho' \leq 2$, the following formulation is used:

$$\tilde{B}_{z,\text{fl}}(\rho', z') = \frac{1}{\sqrt{z'^2 + (1 + \rho')^2} [z'^2 + (1 - \rho')^2]} \{ \mathcal{E}(k_c) + \rho' [\mathcal{E}(k_c) - 2\mathcal{K}(k_c) + 2\mathcal{D}(k_c)] \}. \quad (80)$$

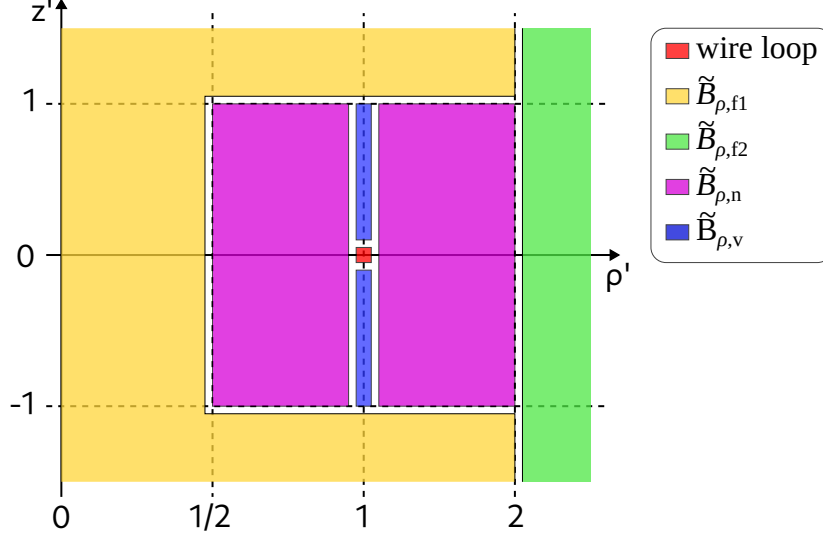


Figure 7: Domain decomposition used to partition the evaluation region for computing \tilde{B}_z accurately. The colored regions indicate at which evaluation locations (ρ', z') which formulation (see legend) is used.

A second far-field method is needed for points with $\rho' > 2$:

$$\tilde{B}_{z,f2}(\rho', z') = \frac{1}{\sqrt{t_1 + t_2}(t_1 - t_2)\rho'^3} \left\{ \mathcal{E}(k_c) + \frac{4}{\alpha_{cd}} [\mathcal{C}(k_c) - \mathcal{D}(k_c)] \right\} \quad (81)$$

with

$$t_1 = \frac{z'^2 + 1}{\rho'^2} + 1 \quad (82)$$

$$t_2 = \frac{2}{\rho'} \quad (83)$$

and

$$\alpha_{cd} = 1 + \frac{1}{\rho'} \left[2 + \frac{1}{\rho'} (1 + z'^2) \right]. \quad (84)$$

In the vicinity of the wire loop, but with $z' \neq 0$, the following method is used to compute \tilde{B}_z :

$$\tilde{B}_{z,n}(\rho', z') = \frac{\text{cel}(\sqrt{k_c^2}, k_c^2, 1 + \rho', 1 - \rho')}{|\rho' - 1|^3 \left[\left(\frac{z'}{\rho' - 1} \right)^2 + \left(1 + \frac{2}{\rho' - 1} \right)^2 \right]^{3/2}}. \quad (85)$$

The expression for \tilde{B}_z becomes significantly simpler at $\rho' = 1$, which is considered next:

$$\tilde{B}_{z,v}(z') = \frac{1}{[z'^2 + 4]^{3/2}} \text{cel} \left(\sqrt{k_c^2}, k_c^2, 2, 0 \right) \quad (86)$$

with

$$k_c^2 = \frac{z'^2}{z'^2 + 4}. \quad (87)$$

2.3. Evaluation in Global Coordinates

Evaluation of the magnetic vector potential \mathbf{A} and magnetic field \mathbf{B} produced by the current carriers considered in this work happens in cylindrical coordinates ρ and z in the local coordinate system of the current carriers. It is often more convenient to be able to work in global coordinates. The methods given in this section show how to transform the evaluation location into cylindrical coordinates in the frame of reference of the current carrier and subsequently transform back the magnetostatic quantities into the global coordinate system.

2.3.1. Straight Wire Segment

Figure 8 illustrates the setup for a straight wire segment. The length of

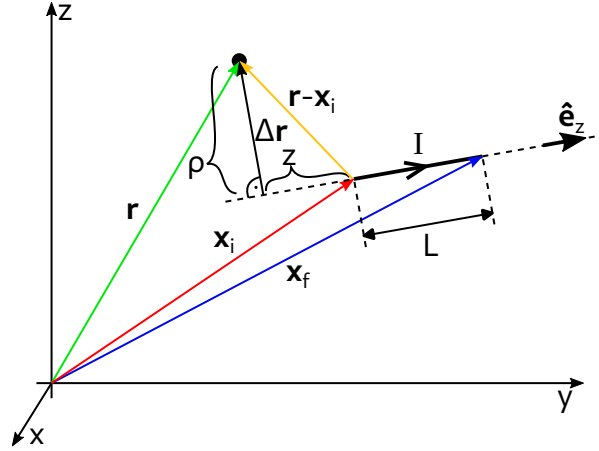


Figure 8: Mapping the components to global coordinates for an exemplary straight wire segment. The wire segment is positioned from \mathbf{x}_i to \mathbf{x}_f . Its parallel unit vector is denoted $\hat{\mathbf{e}}_z$. The length of the wire segment is denoted by L . The evaluation location is denoted by \mathbf{r} .

the wire segment is denoted by L :

$$L = |\mathbf{x}_f - \mathbf{x}_i|. \quad (88)$$

If $L = 0$, no contribution is taken into account from the wire segment. Otherwise, the unit vector along the segment $\hat{\mathbf{e}}_z$ is computed as:

$$\hat{\mathbf{e}}_z = \frac{\mathbf{x}_f - \mathbf{x}_i}{L}. \quad (89)$$

The vertical coordinate z in the coordinate system of the wire segment is:

$$z = (\mathbf{r} - \mathbf{x}_i) \cdot \hat{\mathbf{e}}_z \quad (90)$$

and the normalized z -coordinate is:

$$z' = \frac{z}{L} = \frac{1}{L}(\mathbf{r} - \mathbf{x}_i) \cdot \hat{\mathbf{e}}_z. \quad (91)$$

For the radial coordinate, first the vector $\Delta\mathbf{r}$ is formed:

$$\Delta\mathbf{r} = (\mathbf{r} - \mathbf{x}_i) - z\hat{\mathbf{e}}_z \quad (92)$$

and the radial coordinate ρ is then obtained by taking $\rho = |\Delta\mathbf{r}|$. The normalized radial coordinate ρ' is then obtained as:

$$\rho' = \frac{\rho}{a} = \frac{1}{a}|\mathbf{r} - \mathbf{x}_i - z\hat{\mathbf{e}}_z|. \quad (93)$$

The magnetic vector potential only has a component in parallel direction in the coordinate system of the wire segment. The vector potential of the circular wire loop is thus in Cartesian coordinates:

$$\mathbf{A}(\mathbf{r}) = A_z(\rho', z')\hat{\mathbf{e}}_z. \quad (94)$$

If $\rho' \neq 0$, a unit vector in radial direction is formed as follows:

$$\hat{\mathbf{e}}_\rho = \frac{\Delta\mathbf{r}}{\rho} \quad (95)$$

and the magnetic field of the straight wire segment (consisting only of the tangential component B_φ) is evaluated as:

$$\mathbf{B}(\mathbf{r}) = B_\varphi(\rho', z')\hat{\mathbf{e}}_\varphi \quad (96)$$

with $\hat{\mathbf{e}}_\varphi = \hat{\mathbf{e}}_z \times \hat{\mathbf{e}}_\rho$.

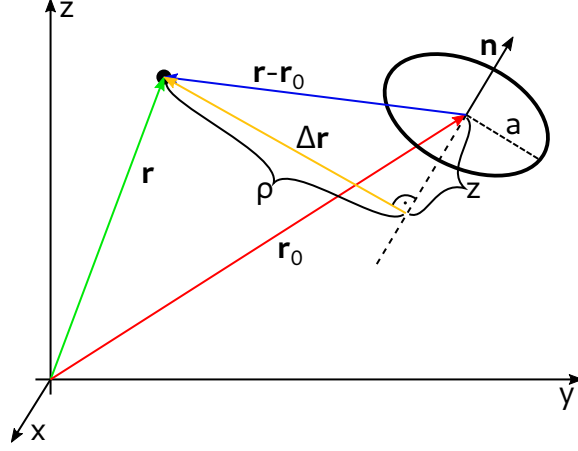


Figure 9: Mapping the components to Cartesian coordinates for an exemplary circular wire loop. The loop is centered around its origin \mathbf{r}_0 . Its normal vector is denoted \mathbf{n} and defines the orientation of the loop. The radius of the loop is denoted by a . The evaluation location is denoted by \mathbf{r} .

2.3.2. Circular Wire Loop

Figure 9 illustrates the setup of a circular wire loop. The z -axis of the coordinate system of the wire loop is defined by the normal vector \mathbf{n} :

$$\hat{\mathbf{e}}_z = \frac{\mathbf{n}}{|\mathbf{n}|}. \quad (97)$$

The z component of the evaluation location is thus obtained as follows:

$$z = (\mathbf{r} - \mathbf{r}_0) \cdot \hat{\mathbf{e}}_z. \quad (98)$$

The normalized z -coordinate z' is then obtained as:

$$z' = \frac{z}{a} = \frac{1}{a}(\mathbf{r} - \mathbf{r}_0) \cdot \hat{\mathbf{e}}_z. \quad (99)$$

For the radial coordinate, first the vector $\Delta\mathbf{r}$ is formed:

$$\Delta\mathbf{r} = (\mathbf{r} - \mathbf{r}_0) - z \hat{\mathbf{e}}_z \quad (100)$$

and the radial coordinate ρ is then obtained by taking $\rho = |\Delta\mathbf{r}|$. The normalized radial coordinate ρ' is then obtained as:

$$\rho' = \frac{\rho}{a} = \frac{1}{a}|(\mathbf{r} - \mathbf{r}_0) - z \hat{\mathbf{e}}_z|. \quad (101)$$

The magnetic field of the circular wire loop consists of two cylindrical components, namely B_ρ and B_z . The Cartesian magnetic field components are then computed as follows:

$$\mathbf{B}(\mathbf{r}) = B_\rho(\rho', z')\hat{\mathbf{e}}_\rho + B_z(\rho', z')\hat{\mathbf{e}}_z. \quad (102)$$

If $\rho' = 0$, only B_z is evaluated. Otherwise, a unit vector in radial direction is formed as follows:

$$\hat{\mathbf{e}}_\rho = \frac{\Delta \mathbf{r}}{\rho} \quad (103)$$

and B_ρ is evaluated as well. The magnetic vector potential only has a component in tangential direction in the coordinate system of the wire loop. It is also only evaluated if $\rho' \neq 0$. The corresponding unit vector $\hat{\mathbf{e}}_\varphi$ is then given by $\hat{\mathbf{e}}_\varphi = \hat{\mathbf{e}}_z \times \hat{\mathbf{e}}_\rho$. The vector potential of the circular wire loop is thus in Cartesian coordinates:

$$\mathbf{A}(\mathbf{r}) = A_\varphi(\rho', z')\hat{\mathbf{e}}_\varphi. \quad (104)$$

2.4. Verification Method

The implementations of above formulas for the magnetic vector potential and magnetic field of a straight wire segment and a circular wire loop need to be tested before using the implementations in routine work. This section introduces the choice of test point coordinates. A rectangular grid of test points in the (ρ', z') -plane is defined, where the choice of knots along the ρ' and z' axes are discussed below. The set of test point coordinates for testing a given current carrier primitive consists of the combinations of all test knots along the ρ' axis with all test knots along the z' axis. Let $T_{\rho'}$ ($T_{z'}$) be the set of knots along the ρ' (z') axis to test the formulation on. Then $T = T_{\rho'} \otimes T_{z'}$ is the set of test point coordinates where \otimes is the cartesian product of two sets and T_{cc} is the subset of points from $T_{\rho'} \otimes T_{z'}$ that are located exactly on the current carrier. First, the choice of test points for testing the implementations of the straight wire segment methods (SWS) is introduced. The set of grid knots along the ρ' axis, $T_{\rho'}^{\text{SWS}}$, are chosen as follows:

- $T_{\rho',1}^{\text{SWS}} = \{0\}$
- $T_{\rho',2}^{\text{SWS}} = \{10^{-30}, 10^{-29}, \dots, 10^{30}\}$

with $T_{\rho'}^{\text{SWS}} = T_{\rho',1}^{\text{SWS}} \cup T_{\rho',2}^{\text{SWS}}$, leading to $|T_{\rho'}^{\text{SWS}}| = 62$. The set of grid knots along the z' axis, $T_{z'}^{\text{SWS}}$, are chosen as follows:

- $T_{z',1}^{\text{SWS}} = \{-10^{30}, -10^{29}, \dots, -10^{-30}\}$
- $T_{z',2}^{\text{SWS}} = \{10^{-30}, 10^{-29}, \dots, 10^{-1}\}$
- $T_{z',3}^{\text{SWS}} = \{1 - 10^{-1}, 1 - 10^{-2}, \dots, 1 - 10^{-15}, 1 - \epsilon_{64}/2\}$
- $T_{z',4}^{\text{SWS}} = \{1 + \epsilon_{64}, 1 + 10^{-15}, 1 + 10^{-14}, \dots, 1 + 10^{-1}\}$
- $T_{z',5}^{\text{SWS}} = \{10^1, 10^2, \dots, 10^{30}\}$
- $T_{z',6}^{\text{SWS}} = \{0, 1/2, 1, 2\}$

with $T_{z'}^{\text{SWS}} = T_{z',1}^{\text{SWS}} \cup T_{z',2}^{\text{SWS}} \cup T_{z',3}^{\text{SWS}} \cup T_{z',4}^{\text{SWS}} \cup T_{z',5}^{\text{SWS}} \cup T_{z',6}^{\text{SWS}}$, leading to $|T_{z'}^{\text{SWS}}| = 157$. The machine-precision epsilon is given by $\epsilon_{64} \approx 2.2 \times 10^{-16}$ for the case of **binary64**. The exclusion of the test points that are located exactly on the wire segment leads to a total number of test point coordinates T_{SWS} for the straight wire segment of $|T_{\text{SWS}}| = 9685$. Next, the choice of test points for testing the implementations of the circular wire loop (CWL) methods is introduced. The set of grid knots along the ρ' axis, $T_{\rho'}^{\text{CWL}}$, are chosen as follows:

- $T_{\rho',1}^{\text{CWL}} = \{10^{-30}, 10^{-29}, \dots, 10^{-1}\}$
- $T_{\rho',2}^{\text{CWL}} = \{1 - 10^{-1}, 1 - 10^{-2}, \dots, 1 - 10^{-15}, 1 - \epsilon_{64}/2\}$
- $T_{\rho',3}^{\text{CWL}} = \{1 + \epsilon_{64}, 1 + 10^{-15}, 1 + 10^{-14}, \dots, 1 + 10^{-1}\}$
- $T_{\rho',4}^{\text{CWL}} = \{10^1, 10^2, \dots, 10^{30}\}$
- $T_{\rho',5}^{\text{CWL}} = \{0, 1/2, 1, 2\}$

with $T_{\rho'}^{\text{CWL}} = T_{\rho',1}^{\text{CWL}} \cup T_{\rho',2}^{\text{CWL}} \cup T_{\rho',3}^{\text{CWL}} \cup T_{\rho',4}^{\text{CWL}} \cup T_{\rho',5}^{\text{CWL}}$, leading to $|T_{\rho'}^{\text{CWL}}| = 96$. The set of grid knots along the z' axis, $T_{z'}^{\text{CWL}}$, are chosen as follows:

- $T_{z',1}^{\text{CWL}} = \{0\}$
- $T_{z',2}^{\text{CWL}} = \{10^{-30}, 10^{-29}, \dots, 10^{30}\}$

with $T_{z'}^{\text{CWL}} = T_{z',1}^{\text{CWL}} \cup T_{z',2}^{\text{CWL}}$, leading to $|T_{z'}^{\text{CWL}}| = 62$. The exclusion of the test point that is located exactly on the wire loop leads to a total number of test point coordinates T_{CWL} for the circular wire loop of $|T_{\text{CWL}}| = 5951$. The reference results are computed on each test point using arbitrary-precision

arithmetic as provided by the Python package `mpmath` [7] and Mathematica [8]. The test point coordinates are computed within the finite-precision test programs used to check the accuracy of the results. This implies that the exact *implied* values of the test point coordinates have to be transported into the arbitrary-precision software used to compute the reference data. The evaluation positions are specified at IEEE754 **binary64** floating-point numbers. The floating point numbers are re-constructed within the arbitrary-precision software in order to properly transport their intended value. In case of **binary64**, this is done as follows for a floating-point number f :

$$f(s, E, M) = \begin{cases} 0 & : E = 0 \text{ and } M = 0 \\ (-1)^s 2^{E-1023} \left(1 + \frac{M}{2^{52}}\right) & : \text{else} \end{cases} \quad (105)$$

where s is the sign bit, E is the exponent specified as an 11-bit unsigned integer and M is the mantissa specified as a 52-bit unsigned integer. Several special cases are defined for certain values of s , E and M , but in the context of this work only the case $E = 0$, $M = 0$ (s arbitrary), which represents an exact zero, is relevant. The organization of those bits in a **binary64** number is shown in Fig. 10. In particular, a test point coordinate value f is passed to

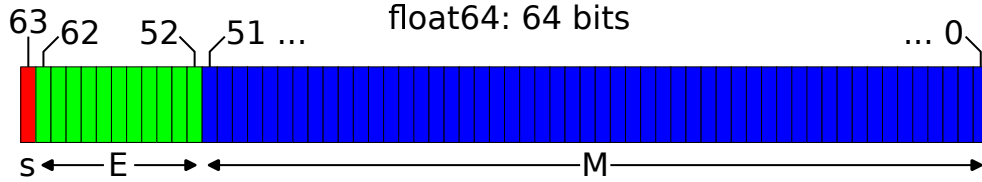


Figure 10: Organization of sign bit s , exponent E (11 bits, unsigned integer) and mantissa M (52 bits, unsigned integer) within the 64 bits of a IEEE754 **binary64** floating-point number. Each box represents one bit and the colors indicate which quantity a bit belongs to (red: sign bit, green: exponent, blue: mantissa).

the reference computation by passing the three values s , E and M as integers (which are easy to represent exactly). Within the reference computation, the value of f is constructed using Eqn. (105) implemented in arbitrary precision and with the exact values of s , E and M . The reference data for the straight wire segment methods is computed using 300 decimal digits of precision. The reference data for the circular wire loop is computed using 200 decimal digits of precision. The evaluation position is specified exactly via s_ρ , E_ρ and M_ρ

(for ρ') and s_z , E_z and M_z (for z'):

$$\begin{aligned}\rho' &\leftarrow \begin{cases} 0 & : E_\rho = 0 \text{ and } M_\rho = 0 \\ (-1)^{s_\rho} 2^{E_\rho-1023} (1 + M_\rho/2^{52}) & : \text{else} \end{cases} \\ z' &\leftarrow \begin{cases} 0 & : E_z = 0 \text{ and } M_z = 0 \\ (-1)^{s_z} 2^{E_z-1023} (1 + M_z/2^{52}) & : \text{else} \end{cases}\end{aligned}$$

The following algorithm is used to compute reference values of \tilde{A}_z and \tilde{B}_φ at (ρ', z') for the straight wire segment:

$$\begin{aligned}r_i &\leftarrow \sqrt{\rho'^2 + z'^2} \\ r_f &\leftarrow \sqrt{\rho'^2 + (1 - z')^2} \\ \epsilon &\leftarrow (r_i + r_f)^{-1} \\ \tilde{A}_z &\leftarrow \text{atanh}(\epsilon)\end{aligned}\tag{106}$$

$$\tilde{B}_\varphi \leftarrow \left(\frac{1}{r_i} + \frac{1}{r_f} \right) \frac{\rho'}{r_i r_f + \rho'^2 + z'(z' - 1)}\tag{107}$$

The following algorithm is used to compute reference values of \tilde{A}_φ and \tilde{B}_ρ at (ρ', z') for the circular wire loop:

$$\begin{aligned}k_c^2 &\leftarrow \frac{z'^2 + (1 - \rho')^2}{z'^2 + (1 + \rho')^2} \\ \tilde{A}_\varphi &\leftarrow \begin{cases} 0 & : \rho' = 0 \\ \frac{1}{\sqrt{z'^2 + (1 + \rho')^2}} \int_0^{\pi/2} \frac{\sin^2(\varphi) - \cos^2(\varphi)}{\sqrt{\cos^2(\varphi) + k_c^2 \sin^2(\varphi)}} d\varphi & : \text{else} \end{cases}\end{aligned}\tag{108}$$

$$\tilde{B}_\rho \leftarrow \begin{cases} 0 & : \rho' = 0 \text{ or } z' = 0 \\ \frac{z'}{[z'^2 + (1 + \rho')^2]^{3/2}} \int_0^{\pi/2} \frac{\sin^2(\varphi) - \cos^2(\varphi)}{[\cos^2(\varphi) + k_c^2 \sin^2(\varphi)]^{3/2}} d\varphi & : \text{else} \end{cases}\tag{109}$$

The method used to compute \tilde{B}_z works slightly differently:

$$k^2 \leftarrow \begin{cases} 4 / \left(\frac{1}{\rho'} + 2 + \rho' \right) & : z' = 0 \\ \frac{4\rho'}{z'^2 + (1+\rho')^2} & : \text{else} \end{cases}$$

$$\tilde{B}_z \leftarrow \frac{1}{[z'^2 + (1 + \rho')^2]^{3/2}} \int_0^{\pi/2} \frac{(1 - \rho') \sin^2(\varphi) + (1 + \rho') \cos^2(\varphi)}{[1 - k^2 \sin^2(\varphi)]^{3/2}} d\varphi \quad (110)$$

The integrals are carried out numerically within the arbitrary-precision software. In case of `mpmath`, double-exponential quadrature [9] is used [10]. The particular choices for the number of digits of precision used throughout the arbitrary-precision computation mentioned above have been adjusted to robustly yield enough equal digits in the outputs from `mpmath` and Mathematica for benchmarking the `binary64` implementation of the methods presented in Sec. 2.1 and 2.2. The error metric employed in this work is given as follows:

$$\delta(a, b) = \begin{cases} \log_{10} \left(\min \left(1, \left| \frac{a-b}{b} \right| \right) \right) & : b \neq 0, a \neq b \\ 0 & : b = 0, a \neq 0 \\ -16 & : \text{else} \end{cases} \quad (111)$$

where the constant -16 is chosen for `binary64` as $\lfloor \log_{10}(\epsilon_{64}) \rfloor$. Here, a is the value to be tested and b is the reference value computed using arbitrary-precision arithmetic.

3. Results

The results of the verification method introduced in Sec. 2.4 are presented next.

3.1. Straight Wire Segment

First, the results of the verification of the straight wire segment methods are presented. The normalized vertical component of the magnetic vector potential, \tilde{A}_z , and the normalized tangential component magnetic field, \tilde{B}_φ , of a straight wire segment have been evaluated using Eqn. (11) and Eqn. (37), respectively, on all test points in T_{SWS} (see Sec. 2.4). The left half of Fig. (11) shows the deviation between the reference data computed for \tilde{A}_z using Eqn. (106) and the results from the **binary64** implementation of Eqn. (11) according to the error metric Eqn. (111). The right half of Fig. (11) shows the corresponding deviation between the reference data computed for \tilde{B}_φ using Eqn. (107) and the results from the **binary64** implementation of Eqn. (37). It is observed that the relative error is less than 10^{-15} for all test points under consideration.

3.2. Circular Wire Loop

Next, the results of the verification of the circular wire loop methods are presented. The normalized tangential component of the magnetic vector potential, \tilde{A}_φ , and the normalized radial and vertical components of the magnetic field, \tilde{B}_ρ and \tilde{B}_z , of a circular wire loop have been evaluated using Eqn. (57), Eqn. (68) and Eqn. (79), respectively, on all test points in T_{CWL} (see Sec. 2.4). Fig. (12) shows the deviation according to the error metric Eqn. (111) between the reference data computed for \tilde{A}_φ using Eqn. (108) and the results from the **binary64** implementation of Eqn. (57). Fig. (13) shows the deviation according to the error metric Eqn. (111) between the reference data computed for \tilde{B}_ρ using Eqn. (109) and the results from the **binary64** implementation of Eqn. (68). Fig. (14) shows the deviation according to the error metric Eqn. (111) between the reference data computed for \tilde{B}_z using Eqn. (110) and the results from the **binary64** implementation of Eqn. (79).

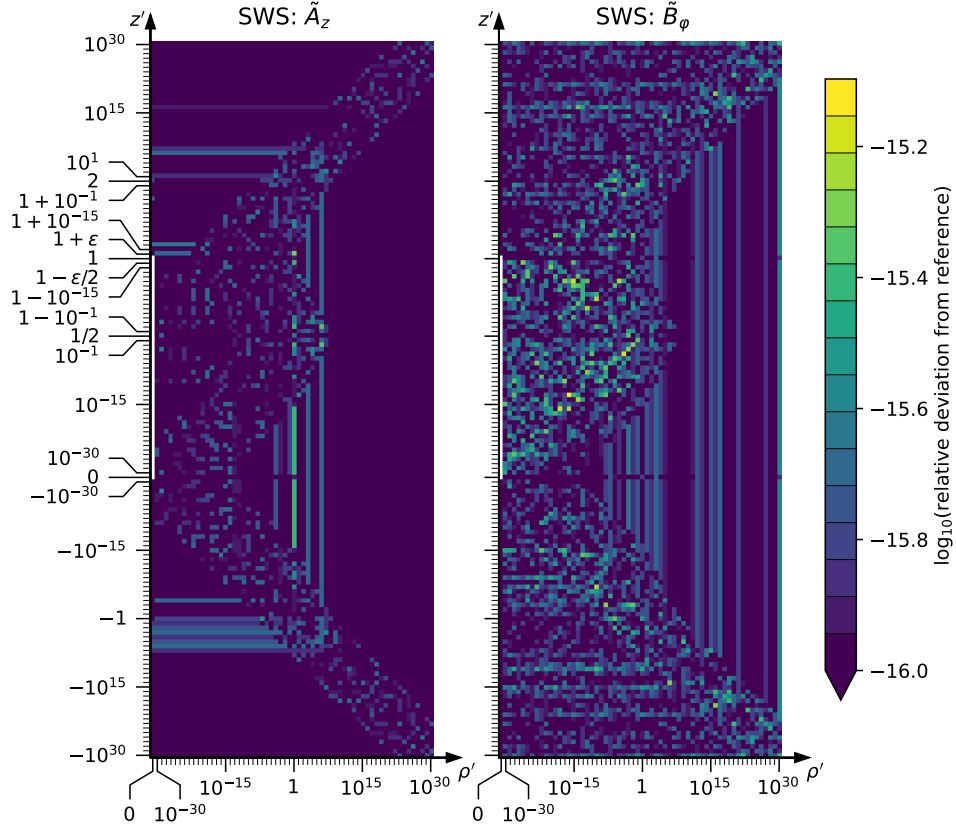


Figure 11: Deviation between the Java implementation of the methods for \tilde{A}_z (left) and \tilde{B}_ϕ (right) of a straight wire segment (SWS). The left plot shows the deviation between the Java implementation of Eqn. (11) and the arbitrary-precision implementation of Eqn. (106) and the right plot shows the deviation between the Java implementation of Eqn. (37) and the arbitrary-precision implementation of Eqn. (107) in the error metric given by Eqn. (111).

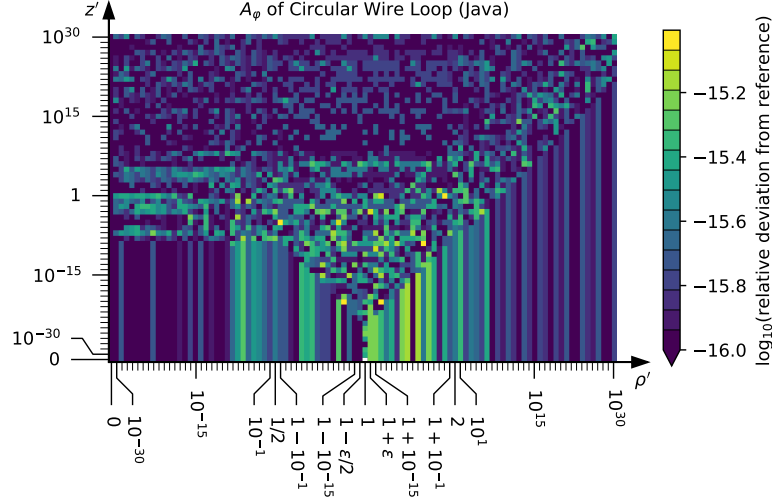


Figure 12: Deviation between Java implementation of Eqn. (57) and Eqn. (108) for the computation of \tilde{A}_φ of a circular wire loop in the error metric given by Eqn. (111).

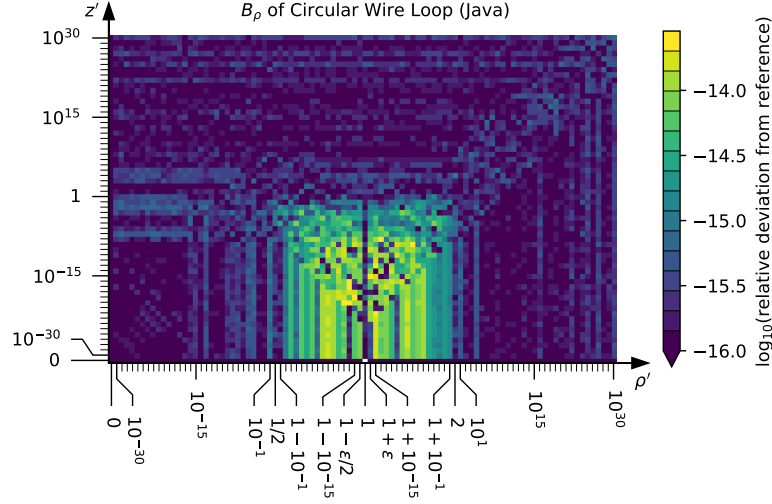


Figure 13: Deviation between Java implementation of Eqn. (68) and Eqn. (109) for the computation of \tilde{B}_ρ of a circular wire loop in the error metric given by Eqn. (111).

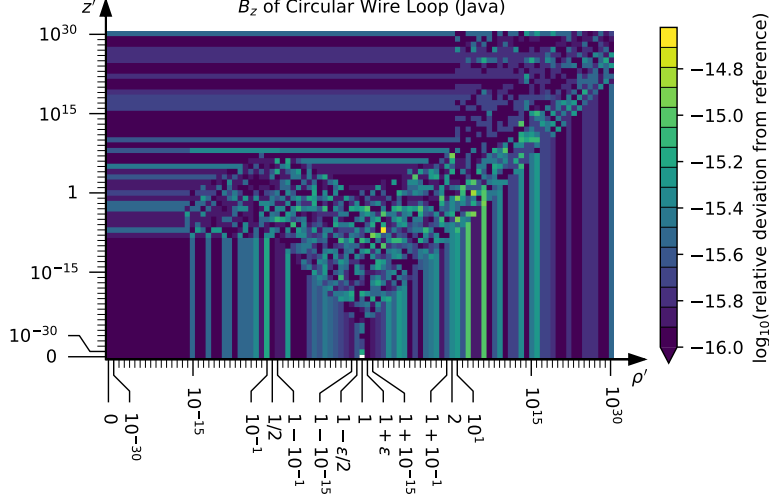


Figure 14: Deviation between Java implementation of Eqn. (79) and Eqn. (110) for the computation of \hat{B}_z of a circular wire loop in the error metric given by Eqn. (111).

3.3. Further tests

Furthermore, it was tested if the methods presented in this work can be used to approximate a circular wire loop by a polygon along the wire down to numerical accuracy. The geometry of the setup is depicted in Fig. (15). The expected result is that the relative deviation between the magnetic field at an arbitrary location from the circular wire loop and from the corresponding polygon approximation using straight wire segments vanishes down to numerical accuracy for a sufficiently large number of points n used to approximate the wire loop. A second-order correction to the polygon approximation for a circular wire loop [11] can be used to improve the approximation. Here, the vertices of the polygon used to approximate the wire loop are adjusted slightly outwards. Figuratively speaking, in the default case (red polygon in Fig. 15) the polygon segments are always inside the wire loop and in the adjusted case (blue polygon in Fig. 15), the polygon segments have portions both inside and outside the wire loop. The results of increasing the number of polygon corners and observing the decay of the relative error between the analytical wire loop expression and the approximation by the polygon are shown in Fig. (16), where the orange graph with + symbols (“on-loop”) denotes the case of the polygon vertices on the loop and the cyan graph with

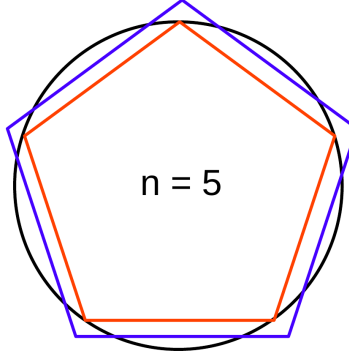


Figure 15: Sketch of the test setup for approximating a circular wire loop by a polygon. The current along the wire loop (black) is approximated by a current along a polygon with vertices either on the loop (red) or vertices adjusted slightly outwards (blue). The case of $n = 5$ vertices used to approximate the loop is shown here.

x symbols (“McGreivy”) denotes the case of the polygon vertices adjusted towards the outside according to Ref. [11]. In those two cases, standard accumulation using the $+=$ operator was used to sum up the contributions from the individual wire segments. It is observed that the results approach numerical accuracy. but then the error grows again if more polygon vertices are used for the approximation. This can be explained by considering that the more vertices are used, the smaller the relative contributions from each individual segment to the total approximation get. If standard accumulation of the results is used, at some number of polygon corners it happens that the remaining contributions are getting smaller than the machine precision epsilon of the current approximation result, thereby effectively ignoring the remaining contributions. Second-order iterative Kahan-Babuska summation [12] had to be used to circumvent this and achieve convergence down to numerical accuracy. This is shown by the red and blue graphs labeled “K-B” in Fig. (16), where the relative deviation from the reference data does not grow as the number of polygon corners is increased beyond the threshold for an accurate approximation.

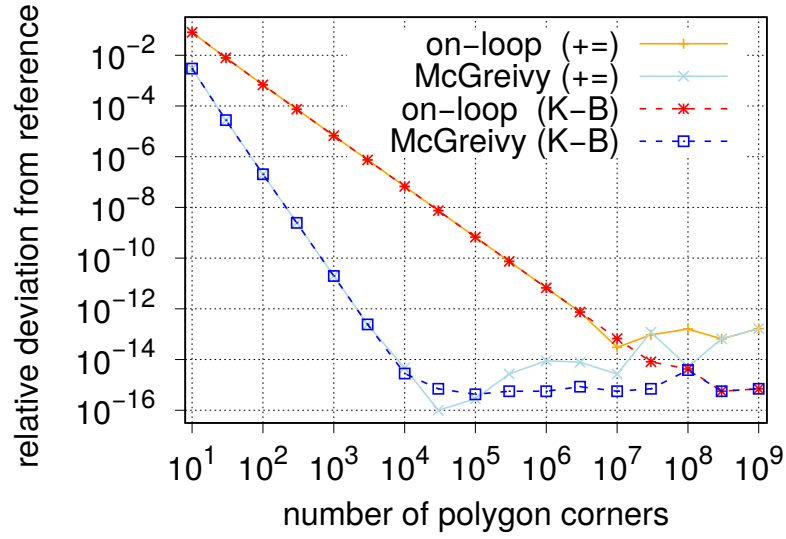


Figure 16: Convergence of the polygon approximation towards the analytical result for the magnetic field of a circular wire loop. The vertices of the polygon used to approximate the wire loop have been put on the wire loop (“on-loop”) as well as adjusted slightly outwards of the loop according to Ref. [11] (“McGreivy”). Standard accumulation using the += operator (“+=”) has been used for the first two graphs (orange and cyan). The second two graphs (red and blue) show the results when the accumulation of the individual contributions is performed using compensated Kahan-Babushka summation [12] (“K-B”).

4. Discussion

Accurate methods have been presented in this work to compute the magnetic vector potential \mathbf{A} and the vacuum magnetic field \mathbf{B} of filamentary current carriers in the form of a straight wire segment and a circular wire loop. Particular attention was paid to make sure that the implemented formulas are capable of achieving nearly full precision of the floating-point arithmetic in which they are implemented. The methods for the straight wire segment achieve 15 out of 16 digits of precision for both the magnetic vector potential and the magnetic field in the `binary64` implementation. The methods for the circular wire loop achieve 15 digits of precision for the magnetic vector potential and for the magnetic field far away from the wire loop. Close to the wire loop, accuracy of the magnetic field methods drops to 14 digits of precision. The reference data was computed using arbitrary-precision arithmetic in two very different implementations (namely the open source `mpmath` Python package and the commercial Mathematica software) and verified to be sufficiently accurate for testing the `binary64` implementations. This reference data is provided along with this article to allow the readers to test their own routines. An application is presented where these methods are used to approximate the magnetic field of a circular current loop by using a current along a polygon aligned with the shape of the wire loop. It is demonstrated that the approximation converges to the analytical result of the wire loop down to machine precision and remains there for further increases in the number of vertices of the approximating polygon. This further demonstrates the robustness of the methods presented in this work. It was found that compensated summation techniques were required in order to correctly accumulate the superposition of a large number of individual polygon segments. The selected second-order Kahan-Babushka summation is therefore used by default in the reference implementation. The asymptotic behaviour of the formulas when evaluating \mathbf{A} and \mathbf{B} close to the current carrier and far away from it is verified to produce the correct results. The free-boundary part of the Variational Moments Equilibrium Code (VMEC) [13] uses interpolation of the vacuum magnetic field produced by the confinement coils of a Stellarator device [14]. It is frequently the case that coils overlap with the region in which the cached interpolation table is computed for further use. During iterations of VMEC, it can happen that this way field values close to the coils enter the computation and it is deemed beneficiary for the robustness of the computation if those values attain the correct asymptotic values.

5. Outlook

An obvious extension of this work is to include gradients of the computed magnetic vector potential and magnetic field. This issue is already discussed in Ref. [15] for the case of the circular wire loop. Precise methods to compute the field gradients would be useful for magnetic field-line tracing applications [16]. Typical applications in experimental physics do not require the full 16 digits of precision provided by a `binary64` implementation of these methods. An implementation in `binary32` arithmetic of the methods presented in this work is expected to achieve a similar fraction of precision, since no constants dependent on machine-precision are used in the implementation. This would correspond to approximately 7 digits of precision that could be expected from a `binary32` implementation. Entry-level graphics processing units (GPUs) (and in particular more advanced models) can perform parallel computations in `binary32` much quicker than regular processors of a PC. The methods presented in this work as well as the gradient methods therefore should be ported to `binary32` and would allow for rapid evaluation at guaranteed error levels still low enough for practical applications in experimental physics. Furthermore, gradient-based optimization methods applied to, e.g., finding the coils for a Stellarator device [17, 18] require calculations of the field gradients. It is noted that derivatives with respect to the position of the current carrier are easily expressed via derivatives of the fields. The change of the field with changing current carrier position is complementary to the change of field with changing evaluation position (relative to the current carrier). It is desirable to have more shapes of current carriers implemented in this framework. In particular, the case of a filamentary arc segment (a segment of a circular wire loop) would be of interest as well as finite-extent current carriers. It is noted that the methods presented by Urankar for this case [19, 20, 21, 22, 23] have recently been reconsidered and improved [24].

6. Acknowledgments

We gratefully acknowledge useful discussions with S. Hudson, C. Zhu, J. Schmitt, S. Lazerson and M. Cianciosa.

This work has been carried out within the framework of the EUROfusion Consortium, funded by the European Union via the Euratom Research and Training Programme (Grant Agreement No 101052200 - EUROfusion). Views and opinions expressed are however those of the author(s) only and do not necessarily reflect those of the European Union or the European Commission. Neither the European Union nor the European Commission can be held responsible for them.

Appendix A. Derivations

The derivations of the formulas presented in Sec. 2 are given here.

Appendix A.1. Straight Wire Segment

The following geometric quantities with $\mathbf{x}_f \equiv \mathbf{x}_{i+1}$ are defined to ease the rest of the derivation:

$$L \equiv |\mathbf{x}_f - \mathbf{x}_i|, \quad (\text{A.1})$$

$$\hat{\mathbf{e}} \equiv (\mathbf{x}_f - \mathbf{x}_i) / L, \quad (\text{A.2})$$

$$\mathbf{R}_i \equiv \mathbf{x} - \mathbf{x}_i, \quad (\text{A.3})$$

$$\mathbf{R}_f \equiv \mathbf{x} - \mathbf{x}_f, \quad (\text{A.4})$$

$$R_i \equiv |\mathbf{R}_i| = |\mathbf{x} - \mathbf{x}_i|, \quad (\text{A.5})$$

$$R_f \equiv |\mathbf{R}_f| = |\mathbf{x} - \mathbf{x}_f|, \quad (\text{A.6})$$

$$R_{i||} \equiv \hat{\mathbf{e}} \cdot \mathbf{R}_i, \quad (\text{A.7})$$

$$R_{f||} \equiv \hat{\mathbf{e}} \cdot \mathbf{R}_f, \quad (\text{A.8})$$

$$\mathbf{R}_\perp \equiv \mathbf{R}_i - R_{i||}\hat{\mathbf{e}}, \quad (\text{A.9})$$

$$R_\perp \equiv |\mathbf{R}_\perp| \quad \text{and} \quad (\text{A.10})$$

$$\mathbf{c}(\lambda) \equiv \mathbf{x}_i + \lambda(\mathbf{x}_f - \mathbf{x}_i) \quad \text{for} \quad 0 \leq \lambda \leq 1. \quad (\text{A.11})$$

The following relations are also needed:

$$L = R_{i||} - R_{f||} \quad (\text{A.12})$$

$$R_i^2 - R_f^2 = L(R_{i||} + R_{f||}) \quad (\text{A.13})$$

$$\Rightarrow R_{i||} = \frac{R_i^2 - R_f^2}{2L} + \frac{L}{2} \quad (\text{A.14})$$

$$\Rightarrow R_{f||} = \frac{R_i^2 - R_f^2}{2L} - \frac{L}{2} \quad (\text{A.15})$$

Appendix A.1.1. Magnetic Vector Potential

The law of Biot and Savart for the magnetic vector potential of a current density distribution $\mathbf{j}(\mathbf{x})$ is as follows [4]:

$$\mathbf{A}(\mathbf{x}) = \frac{\mu_0}{4\pi} \int \frac{\mathbf{j}(\mathbf{x}')}{|\mathbf{x} - \mathbf{x}'|} d\mathbf{x}'. \quad (\text{A.16})$$

The parametrization of points on the line segment $\mathbf{c}(\lambda)$ can be used to apply this to the given geometry of a wire segment:

$$\mathbf{A}(\mathbf{x}) = \frac{\mu_0 I}{4\pi} L \hat{\mathbf{e}} \int_0^1 \frac{d\lambda}{|\mathbf{x} - \mathbf{c}(\lambda)|} \quad (\text{A.17})$$

$$= \frac{\mu_0 I}{4\pi} L \hat{\mathbf{e}} \int_0^1 \frac{d\lambda}{|\mathbf{x} - \mathbf{x}_i - \lambda L \hat{\mathbf{e}}|} . \quad (\text{A.18})$$

A little bit of geometric intuition is needed to simplify the denominator of the integral:

$$\mathbf{x} - \mathbf{x}_i - \lambda L \hat{\mathbf{e}} = \mathbf{R}_i - \lambda L \hat{\mathbf{e}} \quad (\text{A.19})$$

$$= \mathbf{R}_i - R_{i||} \hat{\mathbf{e}} + R_{i||} \hat{\mathbf{e}} - \lambda L \hat{\mathbf{e}} \quad (\text{A.20})$$

$$= \mathbf{R}_i - R_{i||} \hat{\mathbf{e}} + (R_{i||} - \lambda L) \hat{\mathbf{e}} \quad (\text{A.21})$$

$$= \mathbf{R}_\perp + (R_{i||} - \lambda L) \hat{\mathbf{e}} . \quad (\text{A.22})$$

Note that, in particular, $\mathbf{R}_\perp \perp \hat{\mathbf{e}}$ and thus (since $|\hat{\mathbf{e}}| = 1$) due to Pythagoras:

$$|\mathbf{x} - \mathbf{x}_i - \lambda L \hat{\mathbf{e}}|^2 = R_\perp^2 + (R_{i||} - \lambda L)^2 \quad (\text{A.23})$$

and finally with $R_\perp^2 = R_i^2 - R_{i||}^2$ (also due to Pythagoras):

$$|\mathbf{x} - \mathbf{x}_i - \lambda L \hat{\mathbf{e}}|^2 = R_i^2 - R_{i||}^2 + R_{i||}^2 - 2\lambda L R_{i||} + \lambda^2 L^2 \quad (\text{A.24})$$

$$= R_i^2 - 2\lambda L R_{i||} + \lambda^2 L^2 . \quad (\text{A.25})$$

It follows:

$$\mathbf{A}(\mathbf{x}) = \frac{\mu_0 I}{4\pi} L \hat{\mathbf{e}} \int_0^1 \frac{d\lambda}{\sqrt{R_i^2 - 2\lambda L R_{i||} + \lambda^2 L^2}} . \quad (\text{A.26})$$

The following relation holds for $R = a + bx + cx^2$, $\Delta = 4ac - b^2$ with $c > 0$, $2cx + b > \sqrt{-\Delta}$ and $\Delta < 0$ according to integral (2.261) in Ref. [25]:

$$\int \frac{dx}{\sqrt{R}} = \frac{1}{\sqrt{c}} \log \left(2\sqrt{cR} + 2cx + b \right) . \quad (\text{A.27})$$

Here, $x = \lambda$, $a = R_i^2$, $b = -2LR_{i||}$ and $c = L^2$. The corresponding antiderivative of the integrand in Eqn. (A.26) is:

$$\begin{aligned} & \int \frac{d\lambda}{\sqrt{R_i^2 - 2\lambda LR_{i||} + \lambda^2 L^2}} \\ &= \frac{1}{L} \log \left(2\sqrt{L^2 (L^2 \lambda^2 - 2LR_{i||}\lambda + R_i^2)} + 2L^2 \lambda - 2LR_{i||} \right). \end{aligned} \quad (\text{A.28})$$

The definite integral in Eqn. (A.26) is therefore solved by the following expression:

$$\int_0^1 \frac{d\lambda}{\sqrt{R_i^2 - 2\lambda LR_{i||} + \lambda^2 L^2}} \quad (\text{A.29})$$

$$\begin{aligned} &= \frac{1}{L} \left[\log \left(2\sqrt{L^2 (L^2 - 2LR_{i||} + R_i^2)} + 2L^2 - 2LR_{i||} \right) \right. \\ &\quad \left. - \log \left(2\sqrt{L^2 R_i^2 - 2LR_{i||}} \right) \right] \end{aligned} \quad (\text{A.30})$$

$$= \frac{1}{L} \log \left(\frac{2L\sqrt{L^2 - 2LR_{i||} + R_i^2} + 2L^2 - 2LR_{i||}}{2LR_i - 2LR_{i||}} \right) \quad (\text{A.31})$$

Note that

$$L^2 = L(R_{i||} - R_{f||}) \quad (\text{A.32})$$

$$= LR_{i||} - LR_{f||} \quad (\text{A.33})$$

$$\Rightarrow -2LR_{i||} + L^2 = -2LR_{i||} + LR_{i||} - LR_{f||} \quad (\text{A.34})$$

$$= -L(R_{i||} + R_{f||}) \quad (\text{A.35})$$

$$= R_f^2 - R_i^2 \quad (\text{A.36})$$

$$\Rightarrow R_f^2 = R_i^2 - 2LR_{i||} + L^2. \quad (\text{A.37})$$

Therefore:

$$\int_0^1 \frac{d\lambda}{\sqrt{R_i^2 - 2\lambda LR_{i||} + \lambda^2 L^2}} = \frac{1}{L} \log \left(\frac{R_f - R_{f||}}{R_i - R_{i||}} \right). \quad (\text{A.38})$$

Inserting this into Eqn. (A.26) leads to the first intermediate result:

$$\mathbf{A}(\mathbf{x}) = \frac{\mu_0 I}{4\pi} \frac{1}{L} \log \left(\frac{R_f - R_{f||}}{R_i - R_{i||}} \right) \hat{\mathbf{e}} = \frac{\mu_0 I}{4\pi} \log \left(\frac{R_f - R_{f||}}{R_i - R_{i||}} \right) \hat{\mathbf{e}}. \quad (\text{A.39})$$

However, if the point \mathbf{x} is located on the line extension of the wire segment, $R_i = R_{i||}$ and $R_f = R_{f||}$, which leads to a 0/0 division if this formula is directly evaluated. The solution is to cancel the singular term $(L + R_f - R_i)$, which is also zero for points on the line extension of the wire segment, in the numerator and the denominator of Eqn. (A.39). A second look resolves this:

$$\frac{R_f - R_{f||}}{R_i - R_{i||}} = \frac{2L(R_f - R_{f||})}{2L(R_i - R_{i||})} = \frac{2LR_f - 2L\left(\frac{R_i^2 - R_f^2}{2L} - \frac{L}{2}\right)}{2LR_i - 2L\left(\frac{R_i^2 - R_f^2}{2L} + \frac{L}{2}\right)} \quad (\text{A.40})$$

$$= \frac{2LR_f - R_i^2 + R_f^2 + L^2}{2LR_i - R_i^2 + R_f^2 - L^2} \quad (\text{A.41})$$

$$= \frac{2LR_f - R_i^2 + R_f^2 + L^2 + LR_i - LR_i + R_i R_f - R_i R_f}{2LR_i - R_i^2 + R_f^2 - L^2 + LR_f - LR_f + R_i R_f - R_i R_f} \quad (\text{A.42})$$

$$= \frac{\cancel{(L + R_f - R_i)}(R_f + R_i + L)}{\cancel{(L + R_f - R_i)}(R_f + R_i - L)} = \frac{R_f + R_i + L}{R_f + R_i - L}. \quad (\text{A.43})$$

It follows for the vector potential expression:

$$\mathbf{A}(\mathbf{x}) = \frac{\mu_0 I}{4\pi} \log \left(\frac{R_f + R_i + L}{R_f + R_i - L} \right) \hat{\mathbf{e}}. \quad (\text{A.44})$$

The authors of Ref. [2] suggest to normalize the length of the wire segment:

$$\frac{R_f + R_i + L}{R_f + R_i - L} = \frac{1 + \epsilon}{1 - \epsilon} \quad \text{with } \epsilon \equiv \frac{L}{R_i + R_f}, \quad (\text{A.45})$$

leading to

$$\mathbf{A}(\mathbf{x}) = \frac{\mu_0 I}{4\pi} \log \left(\frac{1 + \epsilon}{1 - \epsilon} \right) \hat{\mathbf{e}}. \quad (\text{A.46})$$

This is the result for the magnetic vector potential of a filamentary wire segment presented in Ref. [2]. Note that

$$\text{artanh}(\epsilon) = \frac{1}{2} \log \left(\frac{1 + \epsilon}{1 - \epsilon} \right), \quad (\text{A.47})$$

leading to

$$\mathbf{A}(\mathbf{x}) = \frac{\mu_0 I}{2\pi} \text{artanh}(\epsilon) \hat{\mathbf{e}}. \quad (\text{A.48})$$

Appendix A.1.2. Magnetic Field

The law of Biot and Savart for the magnetic field of a current density distribution $\mathbf{j}(\mathbf{x})$ is as follows [4]:

$$\mathbf{B}(\mathbf{x}) = \frac{\mu_0}{4\pi} \int \mathbf{j}(\mathbf{x}') \times \frac{\mathbf{x} - \mathbf{x}'}{|\mathbf{x} - \mathbf{x}'|^3} d\mathbf{x}'. \quad (\text{A.49})$$

The magnetic field $\mathbf{B}(\mathbf{x})$ is computed from $\mathbf{B} = \nabla \times \mathbf{A}$, applied to Eqn. (A.46). Define

$$f(\epsilon) \equiv \log \left(\frac{1 + \epsilon}{1 - \epsilon} \right) \quad (\text{A.50})$$

and it follows:

$$\frac{4\pi}{\mu_0 I} \mathbf{B} = \nabla \times (f(\epsilon) \hat{\mathbf{e}}) = \nabla f(\epsilon) \times \hat{\mathbf{e}} + f(\epsilon) \underbrace{\nabla \times \hat{\mathbf{e}}}_{=0} = f'(\epsilon) \nabla \epsilon \times \hat{\mathbf{e}}. \quad (\text{A.51})$$

Note that

$$\begin{aligned} \nabla \epsilon &= \nabla \left(\frac{L}{R_i + R_f} \right) = \frac{-L}{(R_i + R_f)^2} (\nabla R_i + \nabla R_f) \\ &= \frac{-L}{(R_i + R_f)^2} \left(\frac{\mathbf{R}_i}{R_i} + \frac{\mathbf{R}_f}{R_f} \right). \end{aligned} \quad (\text{A.52})$$

It follows:

$$\frac{4\pi}{\mu_0 I} \mathbf{B} = f'(\epsilon) \frac{-L}{(R_i + R_f)^2} \left(\frac{\mathbf{R}_i}{R_i} + \frac{\mathbf{R}_f}{R_f} \right) \times \hat{\mathbf{e}} \quad (\text{A.53})$$

$$= f'(\epsilon) \frac{L}{(R_i + R_f)^2} \hat{\mathbf{e}} \times \left(\frac{\mathbf{R}_i}{R_i} + \frac{\mathbf{R}_f}{R_f} \right) \quad (\text{A.54})$$

$$= f'(\epsilon) \frac{\epsilon^2}{L} \hat{\mathbf{e}} \times \left(\frac{\mathbf{R}_i}{R_i} + \frac{\mathbf{R}_f}{R_f} \right). \quad (\text{A.55})$$

Also:

$$\begin{aligned} \frac{\mathbf{R}_i}{R_i} + \frac{\mathbf{R}_f}{R_f} &= \frac{\mathbf{R}_i}{R_i} + \frac{\mathbf{R}_i - L\hat{\mathbf{e}}}{R_f} = \frac{R_f \mathbf{R}_i + R_i(\mathbf{R}_i - L\hat{\mathbf{e}})}{R_i R_f} \\ &= \frac{(R_f + R_i)\mathbf{R}_i + R_i L\hat{\mathbf{e}}}{R_i R_f} = \frac{R_f + R_i}{R_i R_f} \mathbf{R}_i + \frac{R_i L}{R_i R_f} \hat{\mathbf{e}} \end{aligned} \quad (\text{A.56})$$

and therefore:

$$\hat{\mathbf{e}} \times \left(\frac{\mathbf{R}_i}{R_i} + \frac{\mathbf{R}_f}{R_f} \right) = \hat{\mathbf{e}} \times \left(\frac{R_f + R_i}{R_i R_f} \mathbf{R}_i + \frac{R_i L}{R_i R_f} \hat{\mathbf{e}} \right) = \frac{R_f + R_i}{R_i R_f} \hat{\mathbf{e}} \times \mathbf{R}_i, \quad (\text{A.57})$$

since $\hat{\mathbf{e}} \times \hat{\mathbf{e}} = 0$. Inserting this into Eqn. (A.55) leads to:

$$\frac{4\pi}{\mu_0 I} \mathbf{B} = f'(\epsilon) \frac{\epsilon^{\cancel{2}}}{\cancel{R_i} R_f} \hat{\mathbf{e}} \times \mathbf{R}_i = f'(\epsilon) \frac{\epsilon}{R_i R_f} \hat{\mathbf{e}} \times \mathbf{R}_i \quad (\text{A.58})$$

Next, look at $f'(\epsilon)$:

$$f'(\epsilon) = \frac{\cancel{1} - \epsilon}{1 + \epsilon} \frac{1(1 - \epsilon) - (1 + \epsilon)(-1)}{(1 - \epsilon)^{\cancel{2}}} = \frac{1 - \epsilon + 1 + \epsilon}{(1 + \epsilon)(1 - \epsilon)} = \frac{2}{1 - \epsilon^2} \quad (\text{A.59})$$

and insert this into Eqn. (A.58):

$$\frac{4\pi}{\mu_0 I} \mathbf{B} = \frac{2\epsilon}{1 - \epsilon^2} \frac{1}{R_i R_f} \hat{\mathbf{e}} \times \mathbf{R}_i \quad (\text{A.60})$$

$$= \frac{2L}{\cancel{R_i} + R_f} \frac{(R_i + R_f)^{\cancel{2}}}{(R_i + R_f)^2 - L^2} \frac{1}{R_i R_f} \hat{\mathbf{e}} \times \mathbf{R}_i. \quad (\text{A.61})$$

This results in the final expression for the magnetic field:

$$\mathbf{B}(\mathbf{x}) = \frac{\mu_0 I}{4\pi} \frac{2L(R_i + R_f)}{R_i R_f} \frac{1}{(R_i + R_f)^2 - L^2} \hat{\mathbf{e}} \times \mathbf{R}_i. \quad (\text{A.62})$$

Appendix A.2. Circular Wire Loop

The derivation of the circular wire loop formulas is considered next.

Appendix A.2.1. Magnetic Vector Potential

The derivation starts at the expression given by Jackson [4] and listed here in Eqn. (41). Normalized coordinates (ρ', z') as introduced in Eqn. (43) and Eqn. (44) are used to reformulate the expression given by Jackson into the following:

$$A_\varphi(\rho', z') = \frac{\mu_0 I}{\pi} \frac{1}{\sqrt{z'^2 + (1 + \rho')^2}} \left[\frac{(2 - k^2)\mathcal{K}(k) - 2\mathcal{E}(k)}{k^2} \right]. \quad (\text{A.63})$$

A normalizing prefactor is split off according to Eqn. (55). The remaining term $\tilde{A}_\varphi(\rho', z')$ only depends on the geometry of the wire loop and the evaluation location:

$$\tilde{A}_\varphi(\rho', z') = \frac{1}{\sqrt{z'^2 + (1 + \rho')^2}} \left[\frac{(2 - k^2)\mathcal{K}(k) - 2\mathcal{E}(k)}{k^2} \right]. \quad (\text{A.64})$$

Cancellations can happen in the numerical evaluation of Eqn. (A.64) [5]. Therefore, another form for $\tilde{A}_\varphi(\rho', z')$ can be found by employing formulas from Ref. [26] (Section V.B.11 on page 73 therein):

$$\begin{aligned} \mathcal{K}(k) &= \mathcal{E}(k) + k^2 \mathcal{D}(k) \\ \Leftrightarrow \mathcal{D}(k) &= \frac{\mathcal{K}(k) - \mathcal{E}(k)}{k^2} \end{aligned} \quad (\text{A.65})$$

$$\begin{aligned} 2\mathcal{D}(k) &= \mathcal{K}(k) + k^2 \mathcal{C}(k) \\ \Leftrightarrow k^2 \mathcal{C}(k) &= 2\mathcal{D}(k) - \mathcal{K}(k) \\ &= 2 \left(\frac{\mathcal{K}(k) - \mathcal{E}(k)}{k^2} \right) - \mathcal{K}(k) \\ &= \frac{(2 - k^2)\mathcal{K}(k) - 2\mathcal{E}(k)}{k^2}. \end{aligned} \quad (\text{A.66})$$

It is noted that the corresponding expression for \mathcal{C} given in Eqn. (12) of Ref. [15] has a the wrong sign. Application of Eqn. (A.66) to Eqn. (A.64) leads to:

$$\tilde{A}_\varphi(\rho', z') = \frac{k^2}{\sqrt{z'^2 + (1 + \rho')^2}} \mathcal{C}(k). \quad (\text{A.67})$$

This is the far-field method used in Eqn. (58). Note that $\mathcal{C}(k)$ can be evaluated as follows [27, 5]:

$$\begin{aligned} \mathcal{C}(k) &= \text{cel2} \left(\frac{2\sqrt{|k_c|}}{1 + |k_c|}, 0, \frac{2}{(1 + |k_c|)^3} \right) \\ &= \text{cel} \left(\frac{2\sqrt{|k_c|}}{1 + |k_c|}, 1, 0, \frac{2}{(1 + |k_c|)^3} \right). \end{aligned} \quad (\text{A.68})$$

The absolute value around k_c is otherwise omitted in this work because $k_c \geq 0$ always holds for the formulation of k_c used in this work. Eqn. (A.63) is a

linear combination of the complete elliptic integrals of the first and second kind and can be handled by the `cel` function introduced by Bulirsch [5]:

$$\lambda \mathcal{K}(k) + \mu \mathcal{E}(k) = \text{cel}(k_c, 1, \lambda + \mu, \lambda + \mu k_c^2). \quad (\text{A.69})$$

Here, $\lambda = (2 - k^2)/k^2$ and $\mu = -2/k^2$, leading to:

$$\begin{aligned} \lambda + \mu &= \frac{2 - k^2}{k^2} - \frac{2}{k^2} \\ &= \frac{2 - k^2 - 2}{k^2} = -1 \\ \lambda + \mu k_c^2 &= \frac{2 - k^2}{k^2} - \frac{2(1 - k^2)}{k^2} \\ &= \frac{2 - k^2 - 2 + 2k^2}{k^2} = 1 \end{aligned} \quad (\text{A.70})$$

Putting things together, this implies:

$$\frac{(2 - k^2)\mathcal{K}(k) - 2\mathcal{E}(k)}{k^2} = \text{cel}(k_c, 1, -1, 1). \quad (\text{A.71})$$

Thus, $\tilde{A}_\varphi(\rho', z')$ can be expressed as follows:

$$\tilde{A}_\varphi(\rho', z') = \frac{1}{\sqrt{z'^2 + (1 + \rho')^2}} \text{cel}(k_c, 1, -1, 1). \quad (\text{A.72})$$

This is equivalent to Eqn. (3.2.1.6) in Ref. [6]. The near-field (close to $\rho' = 1$) is handled by normalizing terms to $\rho' - 1$:

$$\tilde{A}_\varphi(\rho', z') = \frac{1}{|\rho' - 1| \sqrt{\left(\frac{z'}{\rho' - 1}\right)^2 + \left(1 + \frac{2}{\rho' - 1}\right)^2}} \text{cel}(k_c, 1, -1, 1). \quad (\text{A.73})$$

Introduce n and m with:

$$n \equiv \frac{z'}{\rho' - 1} \quad (\text{A.74})$$

$$m \equiv \frac{\rho' + 1}{\rho' - 1} = 1 + \frac{2}{\rho' - 1} \quad (\text{A.75})$$

where the following was used:

$$\frac{\rho' + 1}{\rho' - 1} = \frac{\rho' - 1 + 2}{\rho' - 1} = 1 + \frac{2}{\rho' - 1}. \quad (\text{A.76})$$

This implies:

$$\tilde{A}_\varphi(\rho', z') = \frac{1}{|\rho' - 1|\sqrt{n^2 + m^2}} \text{cel}(k_c, 1, -1, 1). \quad (\text{A.77})$$

and

$$\begin{aligned} k_c^2 &= \frac{\left(\frac{z'}{\rho'-1}\right)^2 + \left(\frac{\rho'-1}{\rho'-1}\right)^2}{\left(\frac{z'}{\rho'-1}\right)^2 + \left(\frac{\rho'+1}{\rho'-1}\right)^2} \\ &= \frac{n^2 + 1}{n^2 + m^2}. \end{aligned} \quad (\text{A.78})$$

The formulation presented in Eqn. (A.73) is used in Eqn. (60). It remains to derive the special case formulation used in Eqn. (62) for $\rho' = 1$. First, it is noted that inserting $\rho' = 1$ into k_c^2 from Eqn. (49) leads to:

$$k_c^2 = \frac{z'^2}{z'^2 + 4}. \quad (\text{A.79})$$

This implies the following form of the factor in front of cel in Eqn. (A.72) for the case of $\rho' = 1$:

$$\frac{1}{\sqrt{z'^2 + 4}} = \frac{k_c}{|z'|}. \quad (\text{A.80})$$

It follows [5]:

$$\begin{aligned} \tilde{A}_\varphi(\rho' = 1, z') &= \frac{k_c}{|z'|} \text{cel}(k_c, 1, -1, 1) \\ &= \frac{k_c}{|z'|} \int_0^{\pi/2} \frac{\sin^2(\varphi) - \cos^2(\varphi)}{\sqrt{\cos^2(\varphi) + k_c^2 \sin^2(\varphi)}} d\varphi \\ &= \frac{1}{|z'|} \int_0^{\pi/2} \frac{\sin^2(\varphi) - \cos^2(\varphi)}{\sqrt{\sin^2(\varphi) + \frac{1}{k_c^2} \cos^2(\varphi)}} d\varphi. \end{aligned} \quad (\text{A.81})$$

A change of variables is performed from φ to $\beta = \varphi - \pi/2 \Leftrightarrow \varphi = \beta + \pi/2$:

$$\begin{aligned} & \int_0^{\pi/2} \frac{\sin^2(\varphi) - \cos^2(\varphi)}{\sqrt{\sin^2(\varphi) + \frac{1}{k_c^2} \cos^2(\varphi)}} d\varphi \\ &= \int_{-\pi/2}^0 \frac{\sin^2(\beta + \pi/2) - \cos^2(\beta + \pi/2)}{\sqrt{\sin^2(\beta + \pi/2) + \frac{1}{k_c^2} \cos^2(\beta + \pi/2)}} d\beta. \end{aligned} \quad (\text{A.82})$$

The shift in the arguments to sin and cos are incorporated according to:

$$\cos(\beta + \pi/2) = -\sin(\beta) \quad (\text{A.83})$$

$$\sin(\beta + \pi/2) = \cos(\beta). \quad (\text{A.84})$$

This leads to:

$$\begin{aligned} & \int_{-\pi/2}^0 \frac{\sin^2(\beta + \pi/2) - \cos^2(\beta + \pi/2)}{\sqrt{\sin^2(\beta + \pi/2) + \frac{1}{k_c^2} \cos^2(\beta + \pi/2)}} d\beta \\ &= \int_{-\pi/2}^0 \frac{\cos^2(\beta) - \sin^2(\beta)}{\sqrt{\cos^2(\beta) + \frac{1}{k_c^2} \sin^2(\beta)}} d\beta. \end{aligned} \quad (\text{A.85})$$

The limits of the integral are swapped and a negative sign is introduced in order to compensate this:

$$\frac{1}{|z'|} \int_{-\pi/2}^0 \frac{\cos^2(\beta) - \sin^2(\beta)}{\sqrt{\cos^2(\beta) + \frac{1}{k_c^2} \sin^2(\beta)}} d\beta = \frac{-1}{|z'|} \int_0^{-\pi/2} \frac{\cos^2(\beta) - \sin^2(\beta)}{\sqrt{\cos^2(\beta) + \frac{1}{k_c^2} \sin^2(\beta)}} d\beta. \quad (\text{A.86})$$

Another change of variables $\varphi = -\beta$ is performed. This integrand is even-symmetric and thus, the change of variables leads to the following expression:

$$\frac{-1}{|z'|} \int_0^{-\pi/2} \frac{\cos^2(\beta) - \sin^2(\beta)}{\sqrt{\cos^2(\beta) + \frac{1}{k_c^2} \sin^2(\beta)}} d\beta = \frac{1}{|z'|} \int_0^{\pi/2} \frac{\cos^2(\varphi) - \sin^2(\varphi)}{\sqrt{\cos^2(\varphi) + \frac{1}{k_c^2} \sin^2(\varphi)}} d\varphi. \quad (\text{A.87})$$

Note that the negative sign at the front has been incorporated into the sign change of the integration differential. This result can now be evaluated using cel again:

$$\tilde{A}_\varphi(\rho' = 1, z') = \frac{1}{|z'|} \text{cel} \left(\frac{1}{k_c}, 1, 1, -1 \right). \quad (\text{A.88})$$

This is the formulation used in Eqn. (62).

Appendix A.2.2. Magnetic Field

The cylindrical components of the magnetic field are computed from $\mathbf{B} = \nabla \times \mathbf{A}$. The magnetic vector potential \mathbf{A} only has a tangential component A_φ . This implies that the magnetic field only has components in radial (B_ρ) and vertical (B_z) direction:

$$B_\rho = -\frac{\partial A_\varphi}{\partial z} \quad (\text{A.89})$$

$$B_z = \frac{1}{\rho} \frac{\partial(\rho A_\varphi)}{\partial \rho} = \frac{A_\varphi}{\rho} + \frac{\partial A_\varphi}{\partial \rho}. \quad (\text{A.90})$$

The chain rule is applied to the partial derivatives of A_φ in order to take derivatives with respect to the normalized coordinates $\rho' = \rho/a$ and $z' = z/a$, where a is the radius of the wire loop:

$$\frac{\partial A_\varphi}{\partial \rho} = \frac{\partial A_\varphi}{\partial \rho'} \frac{\partial \rho'}{\partial \rho} = \frac{1}{a} \frac{\partial A_\varphi}{\partial \rho'} \quad (\text{A.91})$$

$$\frac{\partial A_\varphi}{\partial z} = \frac{\partial A_\varphi}{\partial z'} \frac{\partial z'}{\partial z} = \frac{1}{a} \frac{\partial A_\varphi}{\partial z'}. \quad (\text{A.92})$$

This implies:

$$B_\rho = -\frac{1}{a} \frac{\partial A_\varphi}{\partial z'} \quad (\text{A.93})$$

$$B_z = \frac{1}{a} \left(\frac{A_\varphi}{\rho'} + \frac{\partial A_\varphi}{\partial \rho'} \right). \quad (\text{A.94})$$

The form of A_φ from Eqn. (55) is inserted into these expressions for the magnetic field components:

$$B_\rho = -\frac{1}{a} \frac{\partial}{\partial z'} \left(\frac{\mu_0 I}{\pi} \tilde{A}_\varphi \right) = -\frac{\mu_0 I}{\pi a} \frac{\partial \tilde{A}_\varphi}{\partial z'} \quad (\text{A.95})$$

$$B_z = \frac{1}{a} \left(\frac{\mu_0 I}{\pi} \frac{\tilde{A}_\varphi}{\rho'} + \frac{\partial}{\partial \rho'} \left(\frac{\mu_0 I}{\pi} \tilde{A}_\varphi \right) \right) = \frac{\mu_0 I}{\pi a} \left(\frac{\tilde{A}_\varphi}{\rho'} + \frac{\partial \tilde{A}_\varphi}{\partial \rho'} \right). \quad (\text{A.96})$$

This allows to define normalized components of the magnetic field:

$$B_\rho = \frac{\mu_0 I}{\pi a} \tilde{B}_\rho \quad (\text{A.97})$$

$$B_z = \frac{\mu_0 I}{\pi a} \tilde{B}_z \quad (\text{A.98})$$

with

$$\tilde{B}_\rho = - \frac{\partial \tilde{A}_\varphi}{\partial z'} \quad (\text{A.99})$$

$$\tilde{B}_z = \frac{\tilde{A}_\varphi}{\rho'} + \frac{\partial \tilde{A}_\varphi}{\partial \rho'}. \quad (\text{A.100})$$

Five derivatives are required in order to formulate the expressions for B_ρ and B_z . They originate from the chain rule and the product rule applied in Eqn. (A.99) and Eqn. (A.100) to the formulation of \tilde{A}_φ in Eqn. (A.72). First, consider the partial derivatives of the factor in front of cel:

$$\begin{aligned} \frac{\partial}{\partial z'} \left(\frac{1}{\sqrt{z'^2 + (1 + \rho')^2}} \right) &= \frac{\partial}{\partial z'} [z'^2 + (1 + \rho')^2]^{-1/2} \\ &= -\frac{1}{2} [z'^2 + (1 + \rho')^2]^{-3/2} 2z' \\ &= \frac{-z'}{[z'^2 + (1 + \rho')^2]^{3/2}} \end{aligned} \quad (\text{A.101})$$

and

$$\begin{aligned} \frac{\partial}{\partial \rho'} \left(\frac{1}{\sqrt{z'^2 + (1 + \rho')^2}} \right) &= \frac{\partial}{\partial \rho'} [z'^2 + (1 + \rho')^2]^{-1/2} \\ &= -\frac{1}{2} [z'^2 + (1 + \rho')^2]^{-3/2} 2(1 + \rho') \\ &= \frac{-(1 + \rho')}{[z'^2 + (1 + \rho')^2]^{3/2}}. \end{aligned} \quad (\text{A.102})$$

The denominator of the integrand in $\text{cel}(k_c, 1, -1, 1)$ is reformulated:

$$\begin{aligned}\text{cel}(k_c, 1, -1, 1) &= \int_0^{\pi/2} \frac{\sin^2 \varphi - \cos^2(\varphi)}{\sqrt{\cos^2(\varphi) + k_c^2 \sin^2(\varphi)}} d\varphi \\ &= \int_0^{\pi/2} \frac{\sin^2 \varphi - \cos^2(\varphi)}{\sqrt{1 - k^2 \sin^2(\varphi)}} d\varphi\end{aligned}\quad (\text{A.103})$$

by using

$$\begin{aligned}\cos^2(\varphi) + k_c^2 \sin^2(\varphi) &= \cos^2(\varphi) + (1 - k^2) \sin^2(\varphi) \\ &= \underbrace{\cos^2(\varphi) + \sin^2(\varphi)}_{=1} - k^2 \sin^2(\varphi) \\ &= 1 - k^2 \sin^2(\varphi).\end{aligned}\quad (\text{A.104})$$

The parameter of $\text{cel}(k_c, 1, -1, 1)$ only appears in the denominator of the integrand. This implies that it suffices to compute the derivative of the denominator in order to compute the derivative of $\text{cel}(k_c, 1, -1, 1)$:

$$\begin{aligned}\frac{\partial}{\partial(k^2)} \left(\frac{1}{\sqrt{1 - k^2 \sin^2(\varphi)}} \right) &= \frac{\partial}{\partial(k^2)} [1 - k^2 \sin^2(\varphi)]^{-1/2} \\ &= -\frac{1}{2} [1 - k^2 \sin^2(\varphi)]^{-3/2} [-\sin^2(\varphi)] \\ &= \frac{1}{2} \frac{\sin^2(\varphi)}{[1 - k^2 \sin^2(\varphi)]^{3/2}}.\end{aligned}\quad (\text{A.105})$$

It follows:

$$\frac{\partial}{\partial(k^2)} \text{cel}(k_c, 1, -1, 1) = \frac{1}{2} \int_0^{\pi/2} \frac{[\sin^2 \varphi - \cos^2(\varphi)] \sin^2(\varphi)}{[1 - k^2 \sin^2(\varphi)]^{3/2}} d\varphi. \quad (\text{A.106})$$

The derivatives of k^2 (see Eqn. (48)) are as follows:

$$\frac{\partial(k^2)}{\partial z'} = \frac{2z'k^2}{z'^2 + (1 + \rho')^2} \quad (\text{A.107})$$

$$\frac{\partial(k^2)}{\partial \rho'} = \frac{1}{z'^2 + (1 + \rho')^2} [4 - k^2 2(1 + \rho')] \quad (\text{A.108})$$

$$= \frac{2[2 - k^2(1 + \rho')]}{z'^2 + (1 + \rho')^2}. \quad (\text{A.109})$$

The next step is to use above five derivatives in deriving the expressions for the normalized cylindrical magnetic field components. First, \tilde{B}_ρ is handled:

$$\begin{aligned}
\tilde{B}_\rho &= -\frac{\partial \tilde{A}_\varphi}{\partial z'} = -\frac{\partial}{\partial z'} \left(\frac{1}{\sqrt{z'^2 + (1 + \rho')^2}} \text{cel}(k_c, 1, -1, 1) \right) \\
&= -\left\{ \frac{\partial}{\partial z'} \left(\frac{1}{\sqrt{z'^2 + (1 + \rho')^2}} \right) \text{cel}(k_c, 1, -1, 1) \right. \\
&\quad \left. + \frac{1}{\sqrt{z'^2 + (1 + \rho')^2}} \frac{\partial [\text{cel}(k_c, 1, -1, 1)]}{\partial(k^2)} \frac{\partial(k^2)}{\partial z'} \right\} \\
&= \frac{z'}{[z'^2 + (1 + \rho')^2]^{3/2}} \text{cel}(k_c, 1, -1, 1) \\
&\quad + \frac{1}{\sqrt{z'^2 + (1 + \rho')^2}} \frac{2z'k^2}{z'^2 + (1 + \rho')^2} \frac{1}{2} \int_0^{\pi/2} \frac{[\sin^2 \varphi - \cos^2(\varphi)] \sin^2(\varphi)}{[1 - k^2 \sin^2(\varphi)]^{3/2}} d\varphi \\
&= \frac{z'}{[z'^2 + (1 + \rho')^2]^{3/2}} \int_0^{\pi/2} \frac{\sin^2 \varphi - \cos^2(\varphi)}{[1 - k^2 \sin^2(\varphi)]^{3/2}} \left[\cancel{1 - k^2 \sin^2(\varphi)} + \cancel{k^2 \sin^2(\varphi)} \right] d\varphi \\
&= \frac{z'}{[z'^2 + (1 + \rho')^2]^{3/2}} \int_0^{\pi/2} \frac{\sin^2 \varphi - \cos^2(\varphi)}{[1 - k^2 \sin^2(\varphi)]^{3/2}} d\varphi \\
&= \frac{z'}{[z'^2 + (1 + \rho')^2]^{3/2}} \text{cel}(k_c, k_c^2, -1, 1). \tag{A.110}
\end{aligned}$$

This is the normalized form of the expression for B_ρ given in Eqn. (3.2.2.4) in Ref. [6]. It is now transformed into a different formulation, which forms the basis for the formulas for B_ρ presented in this work. It holds:

$$\text{cel}(k_c, k_c^2, -1, 1) = \int_0^{\pi/2} \frac{\sin^2 \varphi}{[1 - k^2 \sin^2(\varphi)]^{3/2}} d\varphi - \int_0^{\pi/2} \frac{\cos^2 \varphi}{[1 - k^2 \sin^2(\varphi)]^{3/2}} d\varphi. \tag{A.111}$$

The summands in this equation are reformulated separately. The first term is transformed using the integral (2.584.40) from Ref. [25]:

$$\int_0^{\pi/2} \frac{\sin^2 \varphi}{[1 - k^2 \sin^2(\varphi)]^{3/2}} d\varphi = \frac{1}{k_c^2 k^2} \mathcal{E} - \frac{1}{k^2} \mathcal{K} \quad (\text{A.112})$$

with shorthand notations $\mathcal{E} = \mathcal{E}(k)$ and $\mathcal{K} = \mathcal{K}(k)$. The second term is transformed using the integral (2.584.42) from Ref. [25]:

$$\int_0^{\pi/2} \frac{\cos^2 \varphi}{[1 - k^2 \sin^2(\varphi)]^{3/2}} d\varphi = \frac{1}{k^2} \mathcal{K} - \frac{1}{k^2} \mathcal{E}. \quad (\text{A.113})$$

It follows:

$$\begin{aligned} \text{cel}(k_c, k_c^2, -1, 1) &= \frac{1}{k_c^2 k^2} \mathcal{E} - \frac{1}{k^2} \mathcal{K} - \frac{1}{k^2} \mathcal{K} + \frac{1}{k^2} \mathcal{E} \\ &= \frac{1}{k_c^2} \left[\frac{1 + k_c^2}{k^2} \mathcal{E} - \frac{2k_c^2}{k^2} \mathcal{K} \right] \\ &= \frac{1}{k_c^2} \left[\frac{2 - k^2}{k^2} \mathcal{E} - \frac{2 - 2k^2}{k^2} \mathcal{K} \right] \\ &= \frac{1}{k_c^2} \left[\left(\frac{2}{k^2} - 1 \right) \mathcal{E} + \left(2 - \frac{2}{k^2} \right) \mathcal{K} \right] \\ &= \frac{1}{k_c^2} \left[2\mathcal{K} - \mathcal{E} - 2 \frac{\mathcal{K} - \mathcal{E}}{k^2} \right] \\ &= \frac{1}{k_c^2} [2\mathcal{K} - \mathcal{E} - 2\mathcal{D}] \end{aligned} \quad (\text{A.114})$$

with $\mathcal{D} = \mathcal{D}(k)$. This allows to write \tilde{B}_ρ as follows:

$$\tilde{B}_\rho = \frac{z'}{[z'^2 + (1 + \rho')^2]^{3/2}} \frac{1}{k_c^2} [2\mathcal{K} - \mathcal{E} - 2\mathcal{D}]. \quad (\text{A.115})$$

Furthermore, it is noted that:

$$\begin{aligned} 2\mathcal{K} - \mathcal{E} - 2\mathcal{D} &= k^2 \left[\frac{\mathcal{K} - \mathcal{E}}{k^2} - \frac{2\mathcal{D} - \mathcal{K}}{k^2} \right] \\ &= k^2 (\mathcal{D} - \mathcal{C}). \end{aligned} \quad (\text{A.116})$$

This is used to write \tilde{B}_ρ as follows:

$$\begin{aligned}\tilde{B}_\rho &= \frac{z'}{[z'^2 + (1 + \rho')^2]^{3/2}} \frac{k^2}{k_c^2} (\mathcal{D} - \mathcal{C}) \\ &= \frac{4\rho' z' (\mathcal{D} - \mathcal{C})}{[z'^2 + (1 + \rho')^2]^{3/2} [z'^2 + (1 - \rho')^2]}.\end{aligned}\quad (\text{A.117})$$

This is the form of \tilde{B}_ρ used in Eqn. (69). The near-field formulation is obtained from this by normalizing to $\rho' - 1$:

$$\tilde{B}_\rho = \frac{4\rho' \frac{z'}{|\rho'-1|} (\mathcal{D} - \mathcal{C})}{(\rho' - 1)^4 \left[\left(\frac{z'}{\rho'-1} \right)^2 + \left(1 + \frac{2}{\rho'-1} \right)^2 \right]^{3/2} \left[\left(\frac{z'}{\rho'-1} \right)^2 + 1 \right]}.\quad (\text{A.118})$$

This formulation cannot be used at $\rho' = 1$ close to the wire loop due to the vanishing denominator in that case. Thus, one more formulation is required for \tilde{B}_ρ . The derivation starts from Eqn. (A.115) and $\rho' = 1$ is inserted:

$$\begin{aligned}\tilde{B}_\rho &= \frac{z'}{[z'^2 + 4]^{3/2}} \frac{z'^2 + 4}{z'^2} [2\mathcal{K} - \mathcal{E} - 2\mathcal{D}] \\ &= \frac{1}{z'^2 \sqrt{1 + 4/z'^2}} \frac{z'}{|z'|} [2\mathcal{K} - \mathcal{E} - 2\mathcal{D}]\end{aligned}\quad (\text{A.119})$$

Furthermore:

$$\begin{aligned}2\mathcal{K} - \mathcal{E} - 2\mathcal{D} &= 2\mathcal{K} - \mathcal{E} - 2 \frac{\mathcal{K} - \mathcal{E}}{k^2} \\ &= \left(2 - \frac{2}{k^2} \right) \mathcal{K} + \left(\frac{2}{k^2} - 1 \right) \mathcal{E} \\ &= \left(2 - \frac{2(z'^2 + 4)}{4} \right) \mathcal{K} + \frac{2(z'^2 + 4) - 4}{4} \mathcal{E} \\ &= \frac{4 - z'^2 - 4}{2} \mathcal{K} + \frac{2z'^2 + 8 - 4}{4} \mathcal{E} \\ &= -\frac{1}{2} z'^2 \mathcal{K} + \frac{1}{2} (z'^2 + 2) \mathcal{E}.\end{aligned}\quad (\text{A.120})$$

This allows to write:

$$\tilde{B}_\rho = \frac{k_c}{2} \frac{z'}{|z'|} \left[\left(\frac{2}{z'^2} + 1 \right) \mathcal{E} - \mathcal{K} \right]. \quad (\text{A.121})$$

This is the formulation used in Eqn. (72). In order to derive the vertical component of the magnetic field, \tilde{B}_z , we start again from Eqn. (A.72) for the magnetic vector potential and insert it into Eqn. (A.100):

$$\begin{aligned} \tilde{B}_z &= \frac{1}{\rho' \sqrt{z'^2 + (1 + \rho')^2}} \text{cel}(k_c, 1, -1, 1) \\ &\quad + \frac{\partial}{\partial \rho'} \left[\frac{1}{\sqrt{z'^2 + (1 + \rho')^2}} \text{cel}(k_c, 1, -1, 1) \right] \\ &= \frac{1}{\rho' \sqrt{z'^2 + (1 + \rho')^2}} \text{cel}(k_c, 1, -1, 1) \\ &\quad + \frac{\partial}{\partial \rho'} \left[\frac{1}{\sqrt{z'^2 + (1 + \rho')^2}} \right] \text{cel}(k_c, 1, -1, 1) \\ &\quad + \frac{1}{\sqrt{z'^2 + (1 + \rho')^2}} \frac{\partial}{\partial(k^2)} \text{cel}(k_c, 1, -1, 1) \frac{\partial(k^2)}{\partial \rho'}. \end{aligned} \quad (\text{A.122})$$

Continuing:

$$\begin{aligned} \tilde{B}_z &= \frac{1}{\rho' \sqrt{z'^2 + (1 + \rho')^2}} \text{cel}(k_c, 1, -1, 1) \\ &\quad + \frac{-(1 + \rho')}{[z'^2 + (1 + \rho')^2]^{3/2}} \text{cel}(k_c, 1, -1, 1) \\ &\quad + \frac{1}{\sqrt{z'^2 + (1 + \rho')^2}} \frac{\mathfrak{Z}[2 - k^2(1 + \rho')]}{z'^2 + (1 + \rho')^2} \frac{1}{\mathfrak{Z}} \int_0^{\pi/2} \frac{[\sin^2 \varphi - \cos^2(\varphi)] \sin^2(\varphi)}{[1 - k^2 \sin^2(\varphi)]^{3/2}} d\varphi \\ &= \frac{1}{\rho' \sqrt{z'^2 + (1 + \rho')^2}} \left\{ \int_0^{\pi/2} \frac{\sin^2 \varphi - \cos^2(\varphi)}{\sqrt{1 - k^2 \sin^2(\varphi)}} \left[1 - \frac{\rho'(1 + \rho')}{z'^2 + (1 + \rho')^2} \right] d\varphi \right. \\ &\quad \left. + \frac{\rho'[2 - k^2(1 + \rho')]}{z'^2 + (1 + \rho')^2} \int_0^{\pi/2} \frac{[\sin^2 \varphi - \cos^2(\varphi)] \sin^2 \varphi}{[1 - k^2 \sin^2(\varphi)]^{3/2}} d\varphi \right\} \end{aligned} \quad (\text{A.123})$$

The integrals can be combined to arrive at:

$$\tilde{B}_z = \frac{1}{\rho' \sqrt{z'^2 + (1 + \rho')^2}} \int_0^{\pi/2} \frac{\sin^2 \varphi - \cos^2(\varphi)}{[1 - k^2 \sin^2(\varphi)]^{3/2}} \left\{ [1 - k^2 \sin^2(\varphi)] \left[1 - \frac{\rho'(1 + \rho')}{z'^2 + (1 + \rho')^2} \right] + \frac{\rho' [2 - k^2(1 + \rho')]}{z'^2 + (1 + \rho')^2} \sin^2 \varphi \right\} d\varphi. \quad (\text{A.124})$$

Consider the part inside $\{\}$ in the integrand in more detail:

$$\begin{aligned} & [1 - k^2 \sin^2(\varphi)] \left[1 - \frac{\rho'(1 + \rho')}{z'^2 + (1 + \rho')^2} \right] + \frac{\rho' [2 - k^2(1 + \rho')]}{z'^2 + (1 + \rho')^2} \sin^2 \varphi \\ &= 1 - k^2 \sin^2(\varphi) - \frac{\rho'(1 + \rho')}{z'^2 + (1 + \rho')^2} + \cancel{\frac{\rho' k^2(1 + \rho')}{z'^2 + (1 + \rho')^2} \sin^2 \varphi} \\ & \quad + \underbrace{\frac{2\rho'}{z'^2 + (1 + \rho')^2} \sin^2 \varphi}_{=k^2/2} - \cancel{\frac{\rho' k^2(1 + \rho')}{z'^2 + (1 + \rho')^2} \sin^2 \varphi} \\ &= \frac{1}{2} [1 - k^2 \sin^2 \varphi] + \frac{1}{2} - (1 + \rho') \frac{\rho'}{z'^2 + (1 + \rho')^2} \\ &= \frac{1}{2} [1 - k^2 \sin^2 \varphi] + \frac{1}{2} - (1 + \rho') \frac{1}{4} k^2 \\ &= \frac{1}{2} [1 - k^2 \sin^2 \varphi] + \frac{1}{4} [2 - k^2(1 + \rho')] . \end{aligned} \quad (\text{A.125})$$

Inserting this back into Eqn. (A.124) leads to:

$$\begin{aligned} \tilde{B}_z &= \frac{1}{\rho' \sqrt{z'^2 + (1 + \rho')^2}} \int_0^{\pi/2} \frac{\sin^2 \varphi - \cos^2(\varphi)}{[1 - k^2 \sin^2(\varphi)]^{3/2}} \left\{ \frac{1}{2} [1 - k^2 \sin^2 \varphi] + \frac{1}{4} [2 - k^2(1 + \rho')] \right\} d\varphi \\ &= \frac{1}{\rho' \sqrt{z'^2 + (1 + \rho')^2}} \left\{ \frac{1}{2} \int_0^{\pi/2} \frac{\sin^2 \varphi - \cos^2(\varphi)}{\sqrt{1 - k^2 \sin^2(\varphi)}} d\varphi \right. \\ & \quad \left. + \frac{1}{4} [2 - k^2(1 + \rho')] \int_0^{\pi/2} \frac{\sin^2 \varphi - \cos^2(\varphi)}{[1 - k^2 \sin^2(\varphi)]^{3/2}} d\varphi \right\} \end{aligned} \quad (\text{A.126})$$

Here, the two integrals can be re-expressed using cel:

$$\begin{aligned}\tilde{B}_z = & \frac{1}{2\rho'\sqrt{z'^2 + (1 + \rho')^2}} \left[\text{cel}(k_c, 1, -1, 1) \right. \\ & \left. + \frac{1}{2} [2 - k^2(1 + \rho')] \text{cel}(k_c, k_c^2, -1, 1) \right].\end{aligned}\quad (\text{A.127})$$

This is the formulation of \tilde{B}_z given as (3.2.2.6) in Ref. [6] with

$$2 - k^2(1 + \rho') = 2 - k^2 - k^2\rho' = 1 + k_c^2 - (1 - k_c^2)\rho'. \quad (\text{A.128})$$

It is now shown how this formulation can be transformed into the formulation provided by Walstrom in Eqn. (17) of Ref. [15]. First, consider:

$$\begin{aligned}k^2 &= \frac{4\rho'}{z'^2 + (1 + \rho')^2} \\ \Leftrightarrow \frac{1}{\rho'} &= \frac{4}{k^2} \frac{1}{z'^2 + (1 + \rho')^2}.\end{aligned}\quad (\text{A.129})$$

Inserting this into Eqn. (A.127) leads to:

$$\begin{aligned}\tilde{B}_z &= \frac{1}{[z'^2 + (1 + \rho')^2]^{3/2}} \frac{2}{k^2} \left\{ -\rho' \frac{k^2}{2} \text{cel}(k_c, k_c^2, -1, 1) \right. \\ &\quad \left. + \text{cel}(k_c, 1, -1, 1) + \frac{1 + k_c^2}{2} \text{cel}(k_c, k_c^2, -1, 1) \right\} \\ &= \frac{1}{[z'^2 + (1 + \rho')^2]^{3/2}} \left\{ -\rho' \text{cel}(k_c, k_c^2, -1, 1) \right. \\ &\quad \left. + \frac{2}{k^2} \left[\text{cel}(k_c, 1, -1, 1) + \frac{1 + k_c^2}{2} \text{cel}(k_c, k_c^2, -1, 1) \right] \right\}\end{aligned}\quad (\text{A.130})$$

Using Eqn. (A.114), this is rewritten has:

$$\begin{aligned} \tilde{B}_z = & \frac{1}{[z'^2 + (1 + \rho')^2]^{3/2}} \left\{ -\rho' \frac{1}{k_c^2} [2\mathcal{K} - \mathcal{E} - 2\mathcal{D}] \right. \\ & \left. + \frac{2}{k^2} \left[\text{cel}(k_c, 1, -1, 1) + \frac{1 + k_c^2}{2} \text{cel}(k_c, k_c^2, -1, 1) \right] \right\} \end{aligned} \quad (\text{A.131})$$

$$\begin{aligned} = & \frac{1}{[z'^2 + (1 + \rho')^2]^{3/2}} \frac{1}{k_c^2} \left\{ -\rho' [2\mathcal{K} - \mathcal{E} - 2\mathcal{D}] \right. \\ & \left. + \frac{2k_c^2}{k^2} \left[\text{cel}(k_c, 1, -1, 1) + \frac{1 + k_c^2}{2} \text{cel}(k_c, k_c^2, -1, 1) \right] \right\}. \end{aligned} \quad (\text{A.132})$$

Consider the following:

$$\begin{aligned} \frac{1}{[z'^2 + (1 + \rho')^2]^{3/2}} \frac{1}{k_c^2} &= \frac{1}{[z'^2 + (1 + \rho')^2]^{3/2}} \frac{z'^2 + (1 + \rho')^2}{z'^2 + (1 - \rho')^2} \\ &= \frac{1}{\sqrt{z'^2 + (1 + \rho')^2} [z'^2 + (1 - \rho')^2]}. \end{aligned} \quad (\text{A.133})$$

This leads to:

$$\begin{aligned} \tilde{B}_z = & \frac{1}{\sqrt{z'^2 + (1 + \rho')^2} [z'^2 + (1 - \rho')^2]} \left\{ -\rho' [2\mathcal{K} - \mathcal{E} - 2\mathcal{D}] \right. \\ & \left. + \underbrace{\frac{2k_c^2}{k^2} \left[\text{cel}(k_c, 1, -1, 1) + \frac{1 + k_c^2}{2} \text{cel}(k_c, k_c^2, -1, 1) \right]}_{\equiv (*)} \right\}. \end{aligned} \quad (\text{A.134})$$

Consider (*) alone for now and use Eqn. (A.71) and Eqn. (A.114):

$$\begin{aligned} (*) &= \frac{k_c^2}{k^2} [2 \text{cel}(k_c, 1, -1, 1) + (1 + k_c^2) \text{cel}(k_c, k_c^2, -1, 1)] \\ &= \frac{1}{k^4} \{ 2(1 - k^2) [(2 - k^2)\mathcal{K} - 2\mathcal{E}] + k^2(2 - k^2) [2\mathcal{K} - \mathcal{E} - 2\mathcal{D}] \} \\ &= \frac{1}{k^4} \{ k^4 \mathcal{E} \} = \mathcal{E}. \end{aligned} \quad (\text{A.135})$$

It follows:

$$\tilde{B}_z = \frac{\mathcal{E} + \rho' [\mathcal{E} - 2\mathcal{K} + 2\mathcal{D}]}{\sqrt{z'^2 + (1 + \rho')^2} [z'^2 + (1 - \rho')^2]}. \quad (\text{A.136})$$

This is equivalent to the formulation presented in Eqn. (17) of Ref. [15], which also is the formulation used to compute \tilde{B}_z in Eqn. (80) of this work. This is normalized to ρ'^2 in the following for evaluation at large values of ρ' . First consider the terms in the denominator of Eqn. (A.136):

$$\begin{aligned}\frac{1}{\rho'^2} [z'^2 + (1 + \rho')^2] &= \frac{1}{\rho'^2} (z'^2 + 1 + 2\rho' + \rho'^2) \\ &= \frac{z'^2 + 1}{\rho'^2} + 1 + \frac{2}{\rho'} = t_1 + t_2 \\ \frac{1}{\rho'^2} [z'^2 + (1 - \rho')^2] &= \frac{1}{\rho'^2} (z'^2 + 1 - 2\rho' + \rho'^2) \\ &= \frac{z'^2 + 1}{\rho'^2} + 1 - \frac{2}{\rho'} = t_1 - t_2\end{aligned}\tag{A.137}$$

with

$$t_1 \equiv \frac{z'^2 + 1}{\rho'^2} + 1\tag{A.138}$$

$$t_2 \equiv \frac{2}{\rho'}.\tag{A.139}$$

It follows:

$$\tilde{B}_z = \frac{\mathcal{E} + \rho' [\mathcal{E} - 2\mathcal{K} + 2\mathcal{D}]}{\sqrt{t_1 + t_2}(t_1 - t_2)\rho'^3}\tag{A.140}$$

and with Eqn. (A.116) we arrive at:

$$\tilde{B}_z = \frac{\mathcal{E} + \rho' k^2 [\mathcal{C} - \mathcal{D}]}{\sqrt{t_1 + t_2}(t_1 - t_2)\rho'^3}.\tag{A.141}$$

Furthermore, it holds:

$$\begin{aligned}\rho' k^2 &= \rho' \frac{4\rho'}{z'^2 + (1 + \rho')^2} \\ &= 4 / \left\{ \frac{1}{\rho'^2} [z'^2 + (1 + \rho')^2] \right\} \\ &= 4 / \left[\left(\frac{z'}{\rho'} \right)^2 + \left(\frac{1 + \rho'}{\rho'} \right)^2 \right] = 4 / \alpha_{\text{cd}}\end{aligned}\tag{A.142}$$

with

$$\begin{aligned}
\alpha_{\text{cd}} &= \frac{z'^2}{\rho'^2} + \frac{1 + 2\rho' + \rho'^2}{\rho'^2} \\
&= \frac{1}{\rho'^2} [\rho'^2 + 2\rho' + 1 + z'^2] \\
&= 1 + \frac{1}{\rho'} \left[2 + \frac{1}{\rho'} (1 + z'^2) \right].
\end{aligned} \tag{A.143}$$

Putting things back together, we arrive at:

$$\tilde{B}_z = \frac{1}{\sqrt{t_1 + t_2}(t_1 - t_2)\rho'^3} \left[\mathcal{E} + \frac{4(\mathcal{C} - \mathcal{D})}{1 + \frac{1}{\rho'} \left[2 + \frac{1}{\rho'} (1 + z'^2) \right]} \right]. \tag{A.144}$$

This is the formulation used in Eqn. (81) of this work. One more formulation of \tilde{B}_z is required for this work. The derivation starts at Eqn. (A.131), which is reformulated using Eqn. (A.135) and Eqn. (A.114) as follows:

$$\begin{aligned}
\tilde{B}_z &= \frac{1}{[z'^2 + (1 + \rho')^2]^{3/2}} \frac{1}{k_c^2} [\mathcal{E} - \rho' (2\mathcal{K} - \mathcal{E} - 2\mathcal{D})] \\
&= \frac{1}{[z'^2 + (1 + \rho')^2]^{3/2}} \left[\frac{1}{k_c^2} \mathcal{E} - \rho' \frac{1}{k_c^2} (2\mathcal{K} - \mathcal{E} - 2\mathcal{D}) \right] \\
&= \frac{1}{[z'^2 + (1 + \rho')^2]^{3/2}} \left[\frac{1}{k_c^2} \mathcal{E} - \rho' \text{cel}(k_c, k_c^2, -1, 1) \right].
\end{aligned} \tag{A.145}$$

Integral (2.584.37) from Ref. [25] is used as follows:

$$\begin{aligned}
\frac{1}{k_c^2} \mathcal{E} &= \int_0^{\pi/2} \frac{1}{[1 - k^2 \sin^2(\varphi)]^{3/2}} d\varphi \\
&= \text{cel}(k_c, k_c^2, 1, 1).
\end{aligned} \tag{A.146}$$

It follows:

$$\tilde{B}_z = \frac{1}{[z'^2 + (1 + \rho')^2]^{3/2}} \text{cel}(k_c, k_c^2, 1 + \rho', 1 - \rho'). \tag{A.147}$$

This is the formulation of \tilde{B}_z consistent with Eqn. (14) of Ref. [15]. The terms in Eqn. (A.147) are now normalized to $\rho' - 1$ for use close to the wire

loop. Then:

$$\begin{aligned} \frac{1}{[z'^2 + (1 + \rho')^2]^{3/2}} &= |\rho' - 1|^{-3} \left[\left(\frac{z'}{\rho' - 1} \right)^2 + \left(\frac{\rho' + 1}{\rho' - 1} \right)^2 \right]^{-3/2} \\ &= |\rho' - 1|^{-3} [n^2 + m^2]^{-3/2} \end{aligned} \quad (\text{A.148})$$

Putting things back together, we arrive at:

$$\tilde{B}_z = \frac{1}{|\rho' - 1|^3 [n^2 + m^2]^{3/2}} \text{cel}(k_c, k_c^2, 1 + \rho', 1 - \rho') \quad (\text{A.149})$$

with $k_c = \sqrt{k_c^2}$ and k_c^2 from Eqn. (A.78). This is the formulation used in Eqn. (85) of this work. Above expression cannot be used to compute \tilde{B}_z close to the wire loop at $\rho' = 1$. Therefore, one final special-case formulation is required. The derivation starts again with Eqn. (A.147) and $\rho' = 1$ is inserted. This leads to:

$$\tilde{B}_z = \frac{1}{[z'^2 + 4]^{3/2}} \text{cel}(k_c, k_c^2, 2, 0) \quad (\text{A.150})$$

with

$$k_c^2 = \frac{z'^2}{z'^2 + 4}. \quad (\text{A.151})$$

This is the formulation used in Eqn. (86) of this work.

References

- [1] IEEE Standard for Floating-Point Arithmetic, Institute of Electrical and Electronics Engineers, New York, 2008, note: Standard 754 - 2008.
- [2] J. D. Hanson, S. P. Hirshman, Compact expressions for the Biot-Savart fields of a filamentary segment, *Physics of Plasmas* 9 (2012) 4410–4412. doi:10.1063/1.1507589.
- [3] R. Dawson, P. Milici, F. Plantevin, Gardener’s hyperbolas and the dragged-point principle, *The American Mathematical Monthly* 128 (10) (2021) 911–921. doi:10.1080/00029890.2021.1982634.
- [4] J. D. Jackson, *Classical Electrodynamics*, 5th Edition, Wiley, New York, NY, 2014.
- [5] R. Bulirsch, Numerical Calculation of Elliptic Integrals and Elliptic Functions. III 13 (1969) 305 – 315. doi:10.1007/BF02165405.
- [6] J. Belcher, S. Olbert, N. Derby, TEAL Physics and Mathematics Documentation, accessed 2021-09-02 (2008).
URL http://web.mit.edu/viz/soft/visualizations/tealsim/downloads/TEAL_Physics_Math.pdf
- [7] F. Johansson, et al., mpmath: a Python library for arbitrary-precision floating-point arithmetic (version 0.18), <http://mpmath.org/> (December 2013).
- [8] Wolfram Research, Inc., *Mathematica*, Version 12.1, Champaign, IL, 2021.
URL <https://www.wolfram.com/mathematica>
- [9] T. Hidetosi, M. Masatake, Double exponential formulas for numerical integration, *Publ. Res. Inst. Math. Sci.* 9 (1973) 721 – 741. doi:10.2977/prims/1195192451.
- [10] F. Johansson, et al., Numerical integration (quadrature) - mpmath 1.2.0 documentation, accessed 2022-05-25.
URL <https://mpmath.org/doc/current/calculus/integration.html>

- [11] N. McGreivy, C. Zhu, L. M. Gunderson, S. R. Hudson, Computation of the Biot-Savart line integral with higher-order convergence using straight segments, *Physics of Plasmas* 28 (2021) 082111. doi:10.1063/5.0058014.
- [12] A. Klein, A Generalized Kahan-Babuska-Summation-Algorithm, *Computing* 76 (2006) 279 – 293. doi:10.1007/s00607-005-0139-x.
- [13] S. Hirshman, W. van Rij, P. Merkel, Three-dimensional free boundary calculations using a spectral Green’s function method, *Computer Physics Communications* 43 (1) (1986) 143–155. doi:10.1016/0010-4655(86)90058-5.
- [14] L. Spitzer, The Stellarator Concept, *Phys. Fluids* 1 (4) (1958) 253–264. doi:10.1063/1.1705883.
- [15] P. L. Walstrom, Algorithms for Computing the Magnetic Field, Vector Potential, and Field Derivatives for Circular Current Loops in Cylindrical Coordinates (2017) LA-UR-17-27619doi:10.2172/1377379.
- [16] S. Bozhenkov, J. Geiger, M. Grahl, J. Kißlinger, A. Werner, R. Wolf, Service oriented architecture for scientific analysis at W7-X. An example of a field line tracer, *Fusion Engineering and Design* 88 (2013) 2997–3006. doi:10.1016/j.fusengdes.2013.07.003.
- [17] C. Zhu, S. R. Hudson, Y. Song, Y. Wan, New method to design stellarator coils without the winding surface, *Nuclear Fusion* 58 (1) (2017) 016008. doi:10.1088/1741-4326/aa8e0a.
- [18] S. Hudson, C. Zhu, D. Pfefferlé, L. Gunderson, Differentiating the shape of stellarator coils with respect to the plasma boundary, *Physics Letters A* 382 (38) (2018) 2732–2737. doi:10.1016/j.physleta.2018.07.016.
- [19] L. Urankar, Vector potential and magnetic field of current-carrying finite arc segment in analytical form, Part I: Filament approximation, *IEEE Transactions on Magnetics* 16 (5) (1980) 1283–1288. doi:10.1109/TMAG.1980.1060864.
- [20] L. Urankar, Vector potential and magnetic field of current-carrying finite arc segment in analytical form, part II: Thin sheet approximation, *IEEE*

- Transactions on Magnetism 18 (3) (1982) 911–917. doi:10.1109/TMAG.1982.1061927.
- [21] L. Urankar, Vector potential and magnetic field of current-carrying finite arc segment in analytical form, Part III: Exact computation for rectangular cross section, IEEE Transactions on Magnetism 18 (6) (1982) 1860–1867. doi:10.1109/TMAG.1982.1062166.
 - [22] L. Urankar, Vector potential and magnetic field of current-carrying finite arc segment in analytical form, part IV: General three-dimensional current density, IEEE Transactions on Magnetism 20 (6) (1984) 2145–2150. doi:10.1109/TMAG.1984.1063579.
 - [23] L. Urankar, Vector potential and magnetic field of current-carrying circular finite arc segment in analytical form. V. Polygon cross section, IEEE Transactions on Magnetism 26 (3) (1990) 1171–1180. doi:10.1109/20.53995.
 - [24] F. Maurer, B. Kawkabani, J. K. Nøland, Rapid 3-D Magnetic Integral Field Computation of Current-Carrying Finite Arc Segments With Rectangular Cross Section, IEEE Transactions on Magnetism 56 (2) (2020) 1–12. doi:10.1109/TMAG.2019.2952078.
 - [25] I. S. Gradshteyn, I. M. Ryzhik, D. Zwillinger, V. Moll, Table of Integrals, Series, and Products, 8th Edition, Academic Press, Amsterdam, 2014.
 - [26] E. Jahnke, F. Emde, Tables of Functions with Formulae and Curves, 4th Edition, Dover Publications, New York, NY, 1945.
 - [27] R. Bulirsch, Numerical Calculation of Elliptic Integrals and Elliptic Functions 7 (1965) 78 – 90. doi:10.1007/BF01397975.